npj | climate and atmospheric science

www.nature.com/npjclimatsci

ARTICLE OPEN

Meteorological flash droughts risk projections based on CMIP6 climate change scenarios

Vijay Sreeparvathy[1,2]✉ and V. V. Srinivas[1,2,3]

Meteorological flash droughts (MFDs) are sub-seasonal-to-seasonal drought phenomena characterized by rapid onset/intensification. This study assesses the changes in trends and hotspot regions of MFDs for the present and five future CMIP6 SSP forcing scenarios (SSP-FS) at global-, continental- and regional-scales. Analysis with 12 GCMs indicates that globally, frequency, duration and severity of MFDs are projected to increase ~20–50%, 20–58%, and 26–62%, respectively, with the highest occurrence probability during the summer season. The MFD hotspot regions appeared prominent in arid and semi-arid zones. MFD exposure risk is projected to exceed ~1.5 folds in most continents, with the highest risk in the Indian sub-continent. Furthermore, in Europe and South America, which are currently less impacted by MFDs, a considerable increase in hotspot regions (~122–127%) is projected under the warmest SSP-FS. The LULC-classes and elevation range most vulnerable to MFDs, and regional potential hydrometeorological drivers that trigger the development of MFDs are identified.

npj Climate and Atmospheric Science (2022)5:77 ; https://doi.org/10.1038/s41612-022-00302-1

INTRODUCTION

Flash drought (FD) is a type of extreme event characterized by rapid intensification of drought/dryness conditions, unlike the conventional drought. The FDs are mostly short-duration, intense drought events causing multifaceted impacts on water resources, agriculture, and ecosystem[1]. Unlike the conventional droughts (i.e., slow-developing droughts), which are mainly attributed to the decline in precipitation, the onset of FDs occurs when low precipitation is accompanied by abnormally high temperature, high winds and/or change in atmospheric radiation. This coupled effect can abruptly raise the evapotranspiration rates and remove the available water from the landscape, favouring the rapid intensification of the water-stressed state, leading to FDs. They can manifest as discrete drought episodes, but may also manifest as a rapid increase in severity from a longer-term drought already in progress. If they are not terminated, they may continue into a period of longer-lasting drought. With the intensification of changing climate and anthropogenic activities, the impacts and uncertainty of drought events are projected to increase considerably in future[2–4]. However, to the best of our knowledge, studies conducted to evaluate the projected changes in impacts of FD events based on the future climate projections are limited.

FDs are broadly classified as heatwave FDs and precipitation deficit FDs[5,6]. Heatwave FDs are mainly attributed to the combined effect of (i) a steep rise in air temperature resulting in increased evapotranspiration and (ii) a decrease in soil moisture due to the rising global warming[6,7]. Precipitation plays a vital role in the intensification of heatwave FDs. However, anomalies in precipitation do not initiate those events which could be triggered irrespective of precipitation forcings. These FDs fall under the agricultural drought category as they are caused due to the depletion of soil moisture and can cause severe crop damage, resulting in substantial economic losses. Conversely, precipitation deficit FDs fall under the meteorological drought category, which is caused due to negative precipitation anomalies mainly attributed to climate change. They cause a decline in evapotranspiration and an increase in temperature anomalies. Thus, the two FDs are initiated and sustained by different physical mechanisms, and the associated negative impacts on various socio-economic sectors are also different.

Recent decades witnessed significant progress in FD research, particularly on heatwave FDs. Various approaches based on soil moisture[6,8–10], meteorological variables[7,11–13] and remote sensing[14–18] have been developed to identify FDs at regional and local scales. Christian et al., 2021[1] attempted to assess the impacts of global-scale agricultural FDs from 1980 to 2015, considering the changes in evaporative stress anomalies from multiple reanalysis datasets. However, there are no studies focused on discerning the global-, continental- and regional-scale impacts of precipitation deficit FDs or meteorological FDs (MFDs) for the present and future climate change scenarios and on identifying potential drivers of MFDs. Predictions/early warnings of MFDs are crucial as they can cause adverse effects on various socio-economic sectors. Hence, this study aims at assessing the global-, continental- and regional-scale changes, trends and hotspot regions in MFDs over 24 climatic zones for the present and future climate change conditions depicted by five CMIP6 (Coupled Model Intercomparison Project) SSP-FS (Shared Socioeconomic Pathways forcing scenarios) (SSP1–1.9, SSP1–2.6, SSP2–4.5, SSP3–7.0 and SSP5–8.5). The study assesses the impacts of MFDs in terms of multiple characteristics (duration, severity, relative frequency, variability, and exposure risk). MFD hotspot regions are also identified using a multivariate FD indicator (MFDI). The vulnerability of different LULC (land-use/landcover) classes and elevation ranges to MFDs is assessed at global scale. Furthermore, the hydrometeorological anomalies and the potential climate drivers/predictors favouring the development and intensification of MFDs at regional scale are identified in this study.

RESULTS

Increasing impacts of MFDs

MFDs were determined following the multi-criteria-based detection procedure using Standardized Antecedent Precipitation

---

[1]Department of Civil Engineering, Indian Institute of Science, Bangalore 560 012, India. [2]Interdisciplinary Centre for Water Research (ICWaR), Indian Institute of Science, Bangalore 560 012, India. [3]Divecha Centre for Climate Change, Indian Institute of Science, Bangalore 560 012, India. ✉email: sreeparvathy@iisc.ac.in

Evapotranspiration Index (SAPEI) described in “Methods” section (subsection ‘Identification of MFDs’). For this purpose, the data (see subsection ‘Study area and data’ in “Methods” section) on predictors (precipitation, maximum and minimum temperatures) of MFD obtained from 12 GCMs (Global Circulation Models) were re-gridded to a common resolution (1.5° × 1.5°) using the bilinear interpolation method. Subsequently, they were bias-corrected (using the CPC observed dataset) considering quantile mapping procedure[19]. Multi-model ensemble (MME) medians of the bias-corrected predictors were also estimated. The accuracy of the MFDs identified in this study is conditional on the accuracy of the predictor variables discerned from the GCM outputs. Hence the agreement between GCMs and the observation dataset was investigated in terms of the (i) variation in zonal spatiotemporal averages[20] and (ii) zonal cumulative distribution of the daily spatial averages (Supplementary Fig. 1), of each bias-corrected variable (precipitation, temperature) for the 24 climate zones (detailed in subsection ‘Study area and data’, “Methods” section) using the base/reference period (1979–2014) datasets. The analysis showed that the bias-corrected 12 individual GCMs and GCM MME were found to be fairly close to those constructed from the observed dataset for different climate zones. Hence the bias-corrected predictors from 12 GCMs and their MME medians were considered to determine the global-scale (for the complete global land area) MFD events for the present (1979–2014) and five future (2015–2100) SSP-FS.

Five characteristics (relative frequency/probability of occurrence, duration, critical severity, spatiotemporal variability, and exposure risk) associated with historical and projected future MFDs were determined using climate simulations from 12 GCMs (Supplementary Table 1) and their MME median (subsection ‘Determination of MFD characteristics’ in “Methods” section). To validate the MFD analysis, three characteristics (duration, critical severity, and percentage area experiencing MFDs) were determined for grids covering the global land area corresponding to the historical period (1979–2014) using the observed (CPC) dataset and climate simulations from the 12 GCMs. The regional average annual estimates of MFD characteristics determined based on the observed dataset were found to be within the 5th and 95th percentile values of the corresponding estimates determined using the 12 GCMs for the majority of the 24 climate zones (Supplementary Fig. 2). It indicates that the 12 GCMs could be considered reliable to arrive at future projections of MFDs.

The MFD characteristics discerned based on the GCM outputs indicated that globally there is an increase in the impact of MFDs with all the future SSP-FS (Fig. 1). The mean duration (relative frequency) of MFD is amplified by approximately 22.2 ± 6.5% (21.2 ± 5.2%) in North America, 88 ± 28.3% (83.3 ± 24.3%) in South America, 73.3 ± 13.3% (65.5 ± 9.1%) in Europe, 51 ± 18.9% (43.8 ± 15%) in Africa, 37.8 ± 16.2% (34 ± 12.8%) in Asia, and 44.2 ± 25.6% (38.5 ± 22.5%) in Australia for different SSP-FS considering the estimates derived using the MME. The corresponding ranges for the projected increase in mean critical severity of MFD in those continents are 28.1 ± 6.3, 89.4 ± 26.4, 71.1 ± 11, 59.4 ± 16.7, 43 ± 16.4, and 51 ± 24.7%, respectively (Supplementary Table 2). South America is likely to experience the highest increase in duration, relative frequency, and critical severity of MFDs for all SSP-FS. The SSP1-1.9 scenario, considered the mildest/optimistic scenario (where global CO_2 emissions are cut to net zero around 2050), shows the least projected change in MFD impacts across all continents. The trends in MFD characteristics were identified at grid-scale using the Mann–Kendall trend test considering a 10% significance level (Fig. 2). The analysis projected the highest percentage increase in MFD-affected areas for Africa with a significant positive trend in duration (15.91 ± 10.2%) and critical severity (17.54 ± 10.78%) of MFDs for all SSP-FS (Supplementary Table 3). Other continents exhibit approximately 0–23% increase in area with a positive trend in duration and critical severity for all SSP-FS. The percentage of areas with a negative trend in those MFD characteristics was considerably low (<5%) for all the continents. There was no significant trend in the annual relative frequency of MFDs for historical and future SSP-FS, as MFDs are most likely to occur utmost twice a year in the peak temperature months. Inter-annual variability of MFDs quantifies the lack of consistency in the annual occurrence of MFDs. The maximum variability (=1) is expected in a scenario where MFDs uniformly occur each year or do not occur during the entire period considered (i.e., occurrence follows a uniform probability distribution). In contrast to the other MFD characteristics, variability is projected to decrease in the future for all SSP-FS, with a maximum decrease for the SSP5-8.5 scenario (Fig. 2i). The decrease in future variability of MFDs could be attributed to the increase in the regular occurrence of MFDs annually.

Zone-wise trend analysis was performed considering each climate zone’s average annual MFD characteristics derived from MME. The analysis showed that the mean annual duration and critical severity of MFDs are increasing in all 24 zones for SSP2–4.5, SSP3–7.0, and SSP5–8.5 scenarios (Fig. 3 and Supplementary Table 4). In SSP1–2.6, all the zones showed an increasing trend in critical severity, and a similar trend is evident in the duration of MFDs, except for four zones (1, 3, 21, and 23). Marginally increasing trend (with p-value < 0.1) is evident in (i) mean annual duration for 12 zones in the historical period and 6 zones in the SSP1–1.9 (mildest) scenario and (ii) critical severity for 13 zones in the historical period and 10 zones in SSP1-1.9 scenario (Supplementary Table 1). Apart from the zones that fall under hyper-arid and arid (i.e., Sahara Desert [Zone-11], central Australia [Zone-23], Southern parts of Africa [Zones-13,14], Eastern parts of Brazil [Zone-10]) climate classes, regions such as the United States and Mexico (Zones-4,5,6), India and Bangladesh (Zone-20), and central Asia (Zone-18) are projected to be the most vulnerable to MFDs in terms of severity, frequency and duration for all the SSP-FS (Fig. 4 and Supplementary Fig. 3). Similarly, with regard to zonal trend, apart from the arid regions, central Asia (Zones-16,17), southern Australia (Zone-24), western Europe (Zone-22), central Africa (Zone-12) and northern parts of the USA (Zone-3) are found to exhibit an increasing trend in severity and duration of MFDs in various SSP-FS. The majority of the zones (>16 zones) exhibit higher interannual variability (>0.5). The zones that exhibit higher variability and relative frequency in MFDs (Zones 10,11,3–5) are considered high-risk zones. This is because the occurrence rate of MFDs in those zones is high, and at the same time, MFDs are highly unpredictable, which can intensify their impacts.

Monthly probability of MFD occurrence

The probability of occurrence/relative frequency of MFD in each month (subsection ‘Determination of MFD characteristics’, “Methods” section) was estimated for all the 1.5° grids covering the global land area. The probability is highest during the summer season for the historical period and future SSP-FS (Fig. 5a). This could be attributed to prolonged dry spells with considerable positive air temperature and negative precipitation anomalies, which rapidly intensify the antecedent dry condition and favour the development of MFDs. The MFDs with no prior warnings can cause large agricultural losses and have the highest impacts on Zaid crops cultivated mainly in the summer months. Moreover, the frequent occurrence of MFDs during hot summers can escalate the irrigation water demands, which can indirectly intensify the depletion of surface and sub-surface water resources. The duration of summer or high-temperature months varies from equator to pole and generally ranges from March to July in the Northern hemisphere and December to March in the southern hemisphere, depending on the location. The probability/relative frequency of observing MFDs in summer months is highest in arid and semi-arid regions. An increase in the probability of MFD occurrence (with respect to the historical period) in different months was

(i) Duration of MFDs

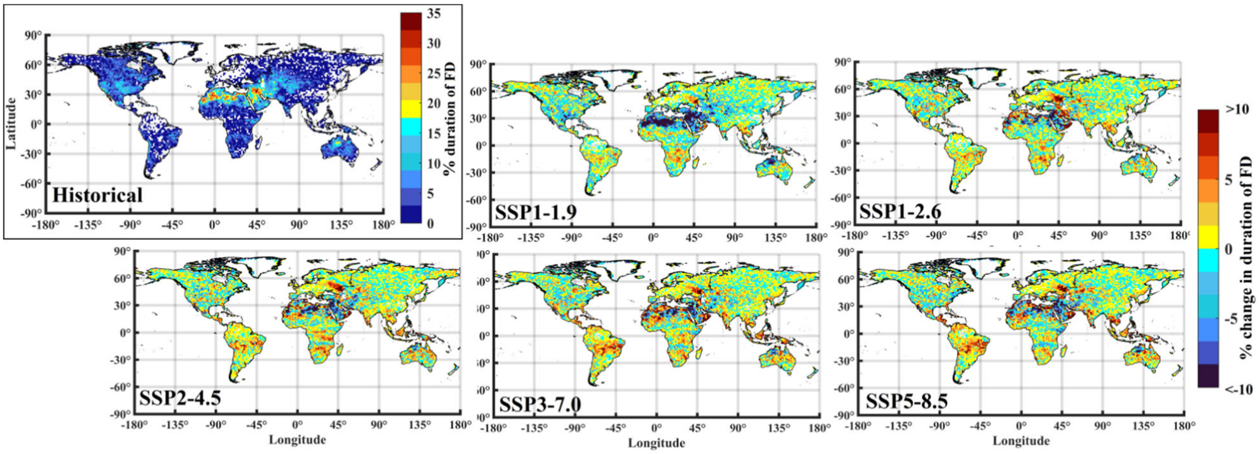

(ii) Critical severity of MFDs

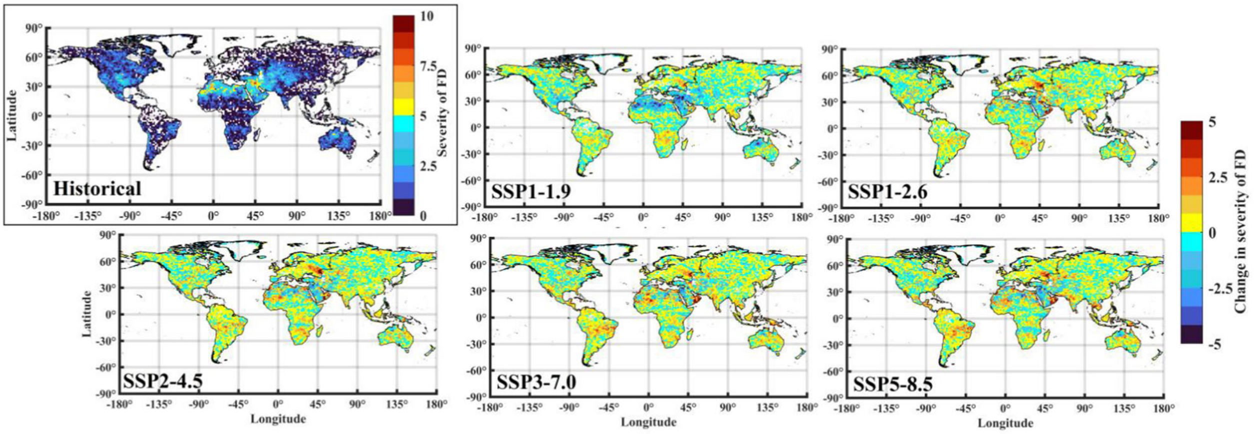

(iii) Relative frequency of MFDs

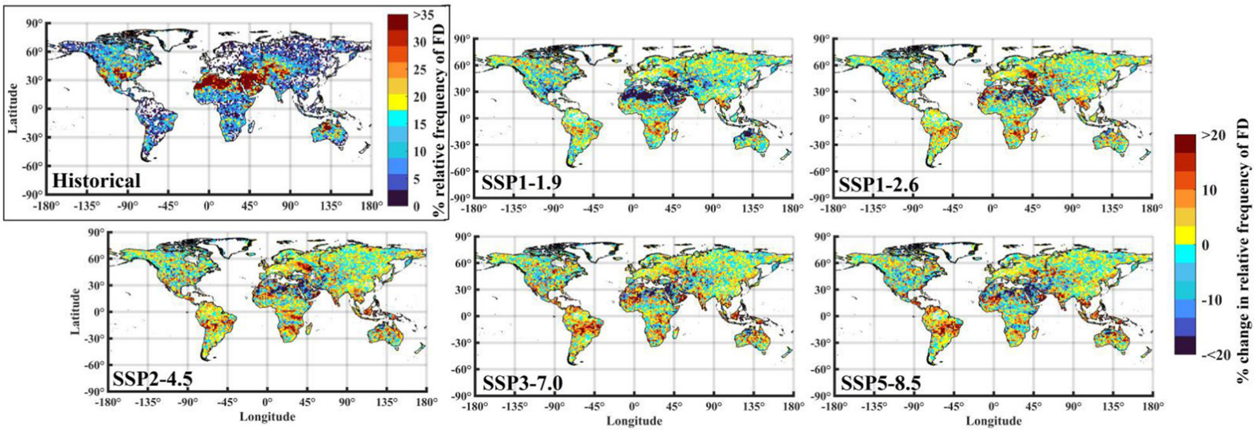

Fig. 1 Global-scale average annual duration, critical severity, and relative frequency of MFDs for the historical period and their changes for future SSP forcing scenarios. Average annual (i) duration, (ii) critical severity, and (iii) relative frequency of MFDs for the historical period and their change for future SSP forcing scenarios. The change is shown in percentage for the duration and relative frequency.

evident in various climate zones for future SSP-FS (Fig. 5b). However, the months that exhibit the highest probability remain unchanged from the past for all SSP-FS. The probability of MFDs in Zone-20 (covering different countries such as Malaysia, Indonesia, Philippines, and Thailand) and Zone-23 (Australia) peak during their respective summer months. However, the probability of observing MFD in other months is closer to that of the peak summer months. This could be possibly attributed to higher anomalies in the occurrence of dry months across years due to the high susceptibility of those regions to increased impacts of anticyclonic events, which inhibit low-level moisture convergence favouring the development of MFDs[21,22].

Intensification of exposure risk with future projections of MFDs

Information on spatio-temporal distribution of the global annual population was considered at 1.5° resolution from resampled

(i) Inter-annual variability of MFDs

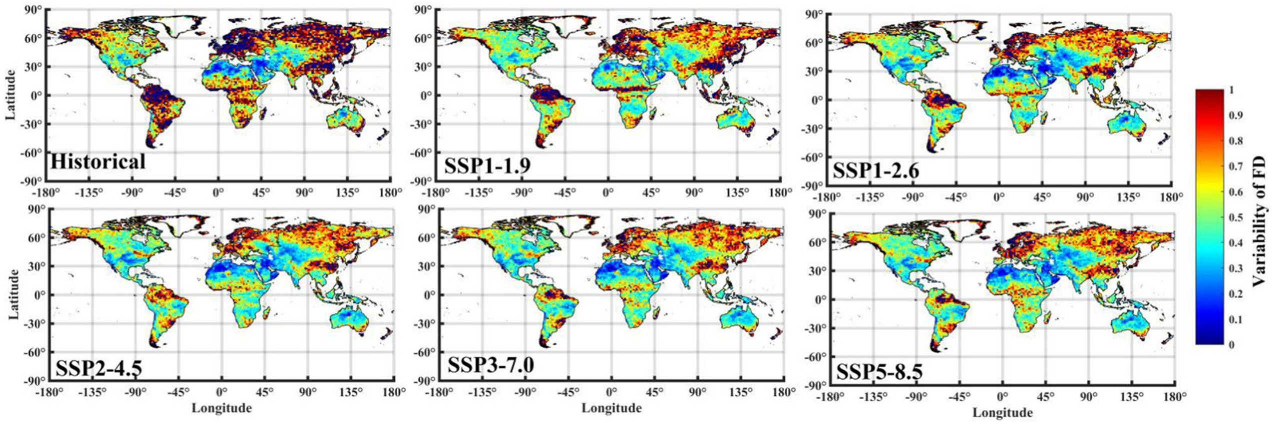

(ii) Trend in duration of MFDs

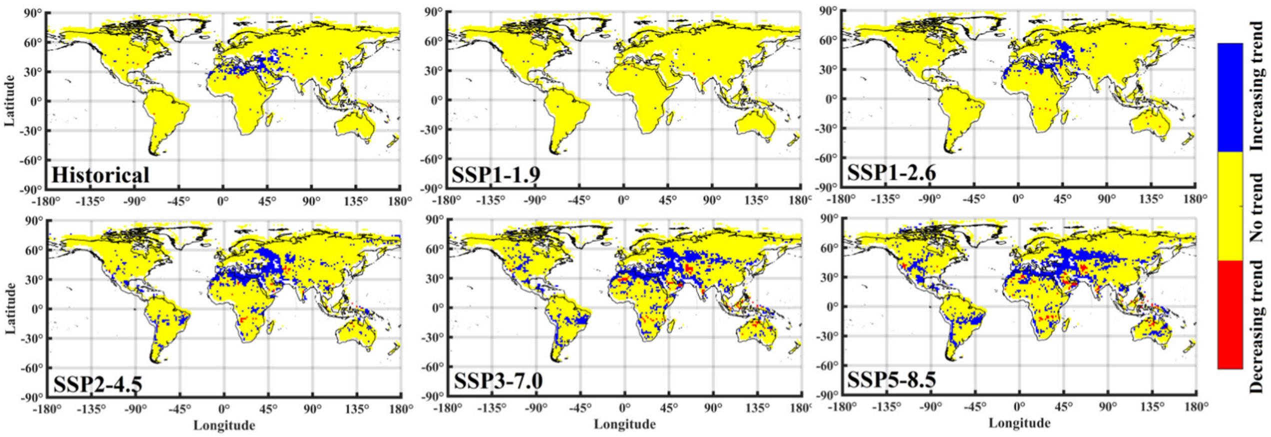

(iii) Trend in critical severity of MFDs

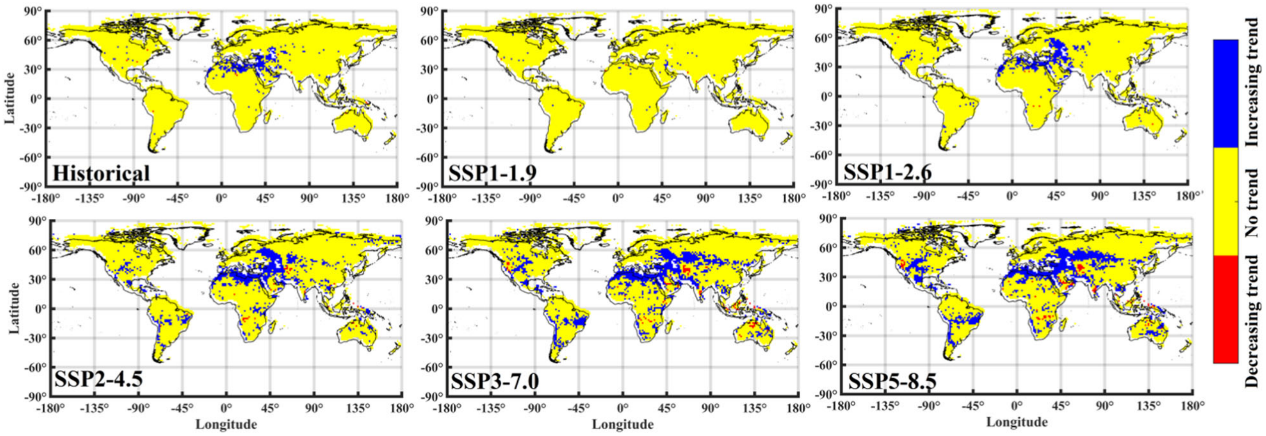

Fig. 2 Global-scale inter-annual variability, and trends in annual estimates of duration and critical severity of MFDs for historical and future SSP forcing scenarios. (i) Inter-annual variability, and trends in annual estimates of (ii) duration and (iii) critical severity of MFDs for historical and future SSP forcing scenarios.

ISIMIP-2b[23] for the historical and future periods for SSP-1, −2, −3, and −5 scenarios for estimating the exposure risk (subsection Determination of MFD characteristics, "Methods" section) of MFDs. The estimates of population exposure risk to projected MFDs for 5 SSP-FS were compared with the corresponding estimates obtained for the 25-year historical period (1981–2005) (Supplementary Fig. 4). The accuracy of the exposure risk estimated in this study is conditional on the accuracy of the population data extracted from the ISMIP-2b. The analysis showed that the average global exposure risk is projected to increase considerably across all SSP-FS for three-time windows: (i) 1.52 ± 0.28 folds for 2026–2050, (ii) 2.75 ± 0.64 folds for 2051–2075, and (iii) 4.74 ± 2.54 folds for 2076–2100. This could be attributed to population growth, LULC changes, and/or increased GHG (Greenhouse Gas) emissions. At the continental scale, the risk is projected to increase with time by more than 1.5 folds in the majority of the SSP-FS, with the highest risk for Africa. Australia is projected to experience high risk (3–14 folds increase across the three-time windows) for the

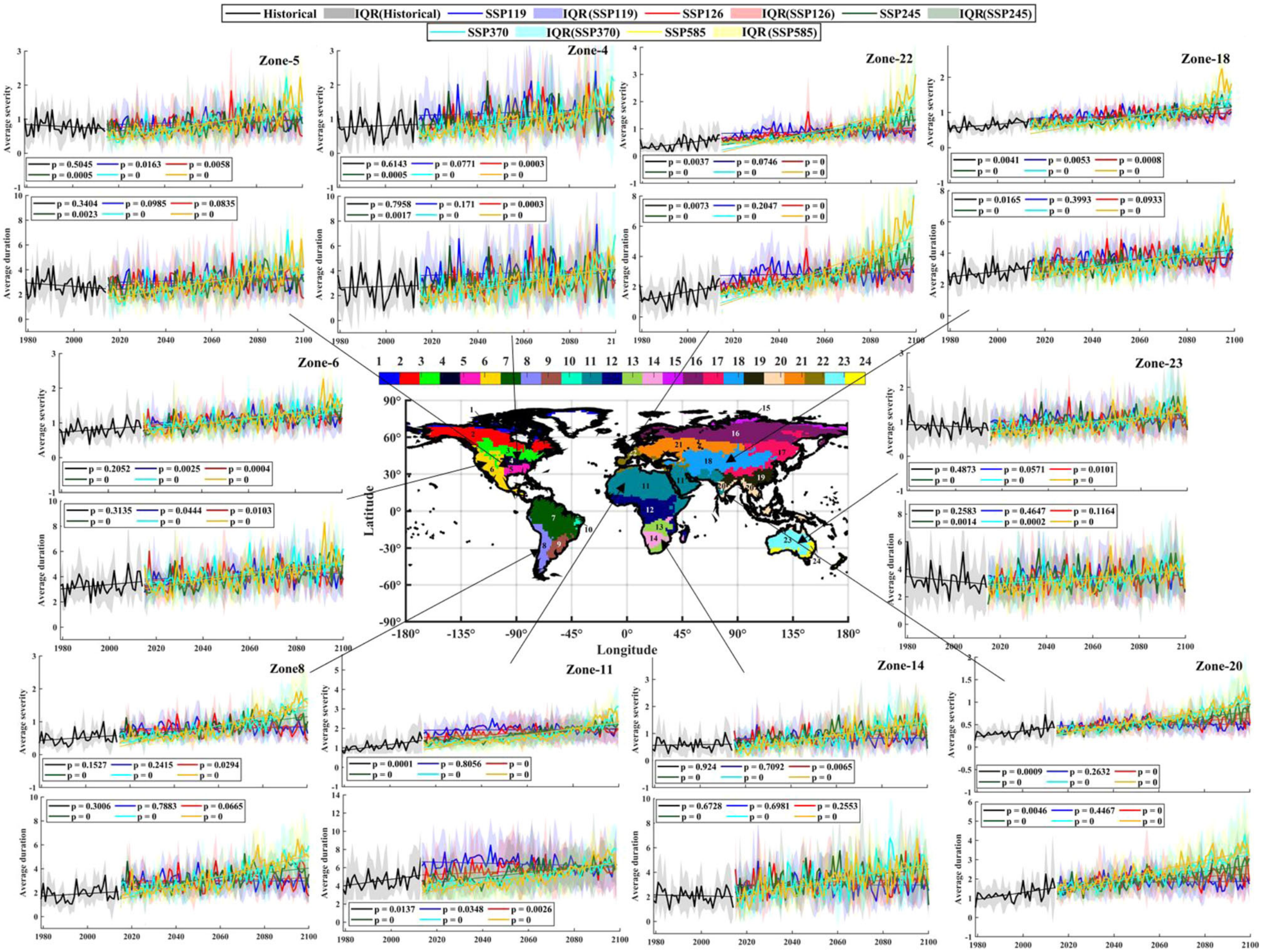

Fig. 3 Regional changes in average annual estimates of duration and critical severity of MFDs for historical and future SSP forcing scenarios for 24 climate zones. Regional changes in average annual estimates of duration and critical severity of MFDs for historical and future SSP forcing scenarios for 24 climate zones. The estimates are based on 12 GCMs, and the multi-model uncertainty is shown as shaded space depicting the confidence interval (CI, mean ± standard deviation). The multi-model ensemble (MME) median corresponding to each scenario is shown as a solid line within their CI. The solid straight line represents the zonal trend of MFDs. The trends are statistically significant for *p*-value less than 0.1. The trends are tested using the Mann–Kendall test considering 10% significance level. The colour legends shown are valid across all the plots.

SSP5–8.5 scenario (Supplementary Table 5). The regional-scale analysis performed on 24 climate zones showed that during the historical period, zones 4 and 5 (eastern parts of USA), 19 (south-eastern parts of China), and 22 (western parts of Europe) experienced the highest exposure risk (Fig. 6). Additionally, zones 2 (Canada), 7 (Columbia, Venezuela, Brazil), 11-14 (Africa), 18 (central Asia), 20 (major portions of India) and 23 (Australia) are expected to be exposed to higher risk in the future period. The Indian sub-continent is the most vulnerable to increased risk across all future SSP-FS due to climate change-induced rise in MFDs and exponential population growth (Supplementary Fig. 4). The large-scale atmospheric and oceanic forcings attributed to climate change have resulted in high variability of summer monsoon in Indian sub-continent[24–26]. The positive sea surface temperature anomalies over the central Pacific Ocean (El Nino) inhibit/weaken the summer monsoon in India, leading to the increased frequency of meteorological droughts[27–30].

Identification of global MFD hotspot regions

Global hotspot regions of MFDs were identified using MFDI (see subsection 'Identification of MFD hotspot regions', "Methods" section), which combines the information of multiple MFD characteristics (relative frequency, duration, critical severity, and exposure risk) considering the MME of GCMs for the historical period and future climate change scenarios (Fig. 7). Europe and South America are projected to have the highest increase in the percentage of the area falling under hotspots of MFDs with respect to the historical period for various SSP-FS (Supplementary Table 6). A slight decline in the hotspot area (%) is projected for North America (−9.7 ± 7.1%), which could be possibly due to the decline in the impacts of MFDs, especially in zones 1 and 4 (Supplementary Fig. 3) in future climate change scenarios. Nevertheless, in the southern parts of North America (zones 5, 6), the impacts (quantified in terms of MFDI) of MFDs are projected to increase considerably in future.

The MFD hotspot areas are mainly concentrated in the arid and semi-arid regions. Hence analysis was carried out to assess the influence of aridity on the occurrence rate of MFDs and its subsequent impacts. The results indicated that the impacts and occurrence rate of MFDs are negatively correlated with the aridity index, i.e., MFDI increases with a decrease in aridity index (Supplementary Fig. 5). In almost all future climate change scenarios (SSP1–2.6, SSP2–4.5, SSP3–7.0, SSP5–8.5), the highest expansion of MFD-affected areas is projected to occur in arid regions (i.e., locations with low aridity index values), followed by semi-arid regions. Most zones exhibit lower impacts (in terms of MFDI) of MFDs for scenario

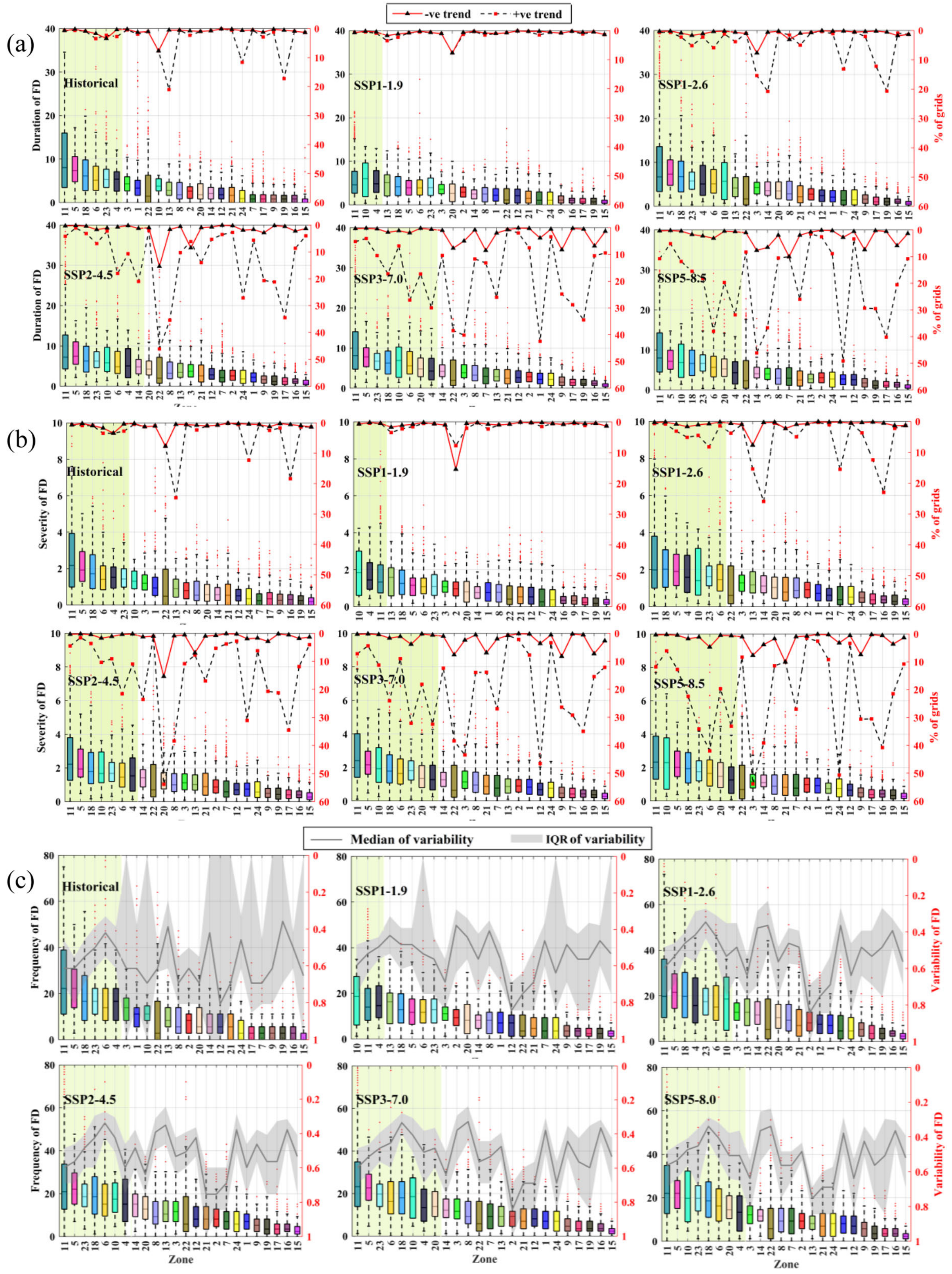

SSP1–1.9, which could be attributed to the increase in aridity index (because of increase in precipitation and lower temperature and hence evapotranspiration due to low GHG emission rate) in these zones during this mildest SSP-FS (Supplementary Fig. 6).

Assessment of the impact of MFDs on various LULC classes and elevation ranges

Prior knowledge of the vulnerability of different LULC patterns and elevation ranges to MFDs is essential for effective planning and

Fig. 4 Variation in estimates of average annual duration, critical severity, and frequency of MFDs across grids in each climate zone. Variation in estimates of average annual **a** duration (in days), **b** critical severity, and **c** frequency of MFDs across grids in each climate zone are shown as boxplots which are arranged in descending order of the mean estimate of MFD characteristic (primary vertical axis). The light green shaded area in each subplot highlights the critical zones, which are those with mean values (of boxplots) of average annual duration, critical severity, and frequency exceeding 10 days, 1.5 and 15, respectively. The percentage of grids exhibiting trends in annual **a** duration and **b** critical severity is shown as line plots (secondary vertical axis). Lines exhibiting negative and positive trends appear as solid and dotted lines, respectively. **c** Median inter-annual variability index of MFDs (secondary vertical axis) for each climate zone is shown as the solid line within the grey-shaded area. The grey-shaded region represents the inter-quartile range (IQR) of inter-annual variability index values across grids in each zone. The MFD characteristics were identified based on the multi-model ensemble. The whiskers of the boxplots extend from 5% and 95% quantiles on the lower and the upper side of the box, respectively. The horizontal line in the box represents the median, whereas the red dots represent outliers.

implementing MFD mitigation activities. For this purpose, the elevation and LULC data of the global land area were extracted from SRTM-DEM and CGLS-LC, respectively. It is to be noted that the inferences drawn on the influence of LULC classes and elevation ranges are conditional on the overall accuracy of CGLS-LC and SRTM-DEM data. The overall accuracy of the CGLS-LC discrete global LC map is found to be 80.6 ± 0.7% at a 95% confidence level[31]. The global scale MFDI (see subsection 'Identification of MFD hotspot regions', "Methods" section) estimates were recalculated considering all the MFD characteristics (relative frequency, duration, critical severity) except exposure risk to ignore the effect of population. The MFDIs were calculated for historical and future SSP-FS to assess the influence of elevation ranges, whereas only the historical period was considered to evaluate the influence of LULC classes on MFDs. This is mainly because LULC classes are susceptible to significant changes in the future climate change scenario. The estimated MFDIs were visualized in the form of 1.5° resolution gridded raster images. The image was then resampled to have the same spatial extent and origin as that of the (i) 30 m resolution SRTM-DEM and (ii) 100 m resolution LULC map to extract information on MFDI for all the pixels covering the global land area.

Variations of MFDI (for the historical period) corresponding to pixels of each of the 10 LULC classes across the globe were visualized in the form of boxplots (Fig. 8a). The analysis showed that susceptibility to MFDs is (i) least for herbaceous wetlands and forested (open and closed forest) LULC classes and (ii) highest for bare vegetation LULC class. This is mainly because herbaceous wetlands and forested areas have high soil water retention properties, unlike bare vegetation. Moreover, dense vegetation typically affects the surface albedo by absorbing more heat than bare vegetation. These warm conditions transport moisture from the forest to the atmosphere, accelerating the condensation process and resulting in increased precipitation. Furthermore, dense vegetation reduces the local temperature. It blocks the incoming daytime solar radiation due to the shading effect. This reduces the absorption and storage of short-wave radiation at the ground surface and the reemission of long-wave radiation from the surface to the atmosphere, thereby lowering the local air temperature[32–34].

The variation of global MFDI with elevation was evaluated by considering a zone-wise joint probability density plot (Fig. 8b). The joint probability density of MFDI and elevation was determined using the Kernel density estimation (KDE) method. Further, zone-wise inferences were drawn from its corresponding plot. The analysis showed that in the majority of the 24 zones, the probability of experiencing high-impact MFDs (quantified using MFDI values) is highest in the lower elevation ranges (<1000 m) for the historical period and future SSP-FS. Anomalies in this general behaviour existed in zones 6, 13, 14, and 18, which exhibited higher probabilities of experiencing high impact MFDs at larger elevation ranges.

Hydrometeorological drivers of MFDs

The MFDs are initiated primarily due to the aberrant precipitation variations and/or anomalous increase in atmospheric evaporative demand due to increased temperature anomalies[5,11]. To gain insight into this, anomalies of pentad means of precipitation, potential evapotranspiration (PET), and temperature derived based on climate simulations from multiple GCMs were analyzed. Pentad means of these anomalies were determined for 10 pentads corresponding to each MFD event (5 pentads preceding and another 5 pentads following the initialization of an event) identified at each grid in a chosen region for the period corresponding to each scenario. MFD events were identified based on each of the 12 GCMs considered. The 10 pentad means of the precipitation, PET, and average temperature were standardized to nullify the effect of the difference in their magnitude across grids in the chosen region for the purpose of their comparison. Standardization of values corresponding to a grid involved deducting each value by the grid's climatological pentads mean and then dividing by the grid's pentads standard deviation estimated over the period (i) 1979–2014 in analysis with historical data, and (ii) 2015–2100 in the case of future SSP-FS. Investigations were carried out to analyze the anomalies of precipitation, PET and temperature at regional scale for each of the 24 climate regions. The variation in each of the derived 10 standardized values of pentad mean precipitation, PET, and average temperature corresponding to all the MFDs at grids in a chosen region was analyzed by constructing boxplots. This was done to assess the effect of the hydroclimatic anomalies on the initialization and development of MFDs, as the anomalies trigger the intensification of the antecedent water-stressed state to create the most favourable condition for the development of high-impact MFDs.

The analysis showed that the onset of MFDs is triggered by (i) an increase in the pentad mean temperature and PET anomalies and (ii) an abrupt increase in the anomaly of pentad mean precipitation. Following the onset of a MFD, a monotonic relationship is evident between pentad mean precipitation and temperature or PET anomalies, with values of temperature and PET anomalies increasing and precipitation anomalies decreasing for both historical and SSP-FS (Fig. 9 and Supplementary Fig. 7), as expected. It is found that initiation of MFDs mostly occurs after the onset of summer wet spells, following which the precipitation anomalies begin to dip drastically with continued increasing temperature and PET anomalies favouring the intensification of MFDs (especially during the summer wet spell breaks). As expected, the MFDs are found to cease with the onset of summer wet spells or a drastic decrease in the temperature anomalies. In hyper-arid and arid regions (e.g., 10, 11), even a marginal decline in the precipitation anomalies can initiate MFDs. Hence MFDs are projected to occur more frequently in these regions due to the increased probability of high temperature with below-average annual precipitation and its high inter-annual variability.

A comprehensive understanding of different regional scale hydrometeorological drivers/attributes which influence MFDs is

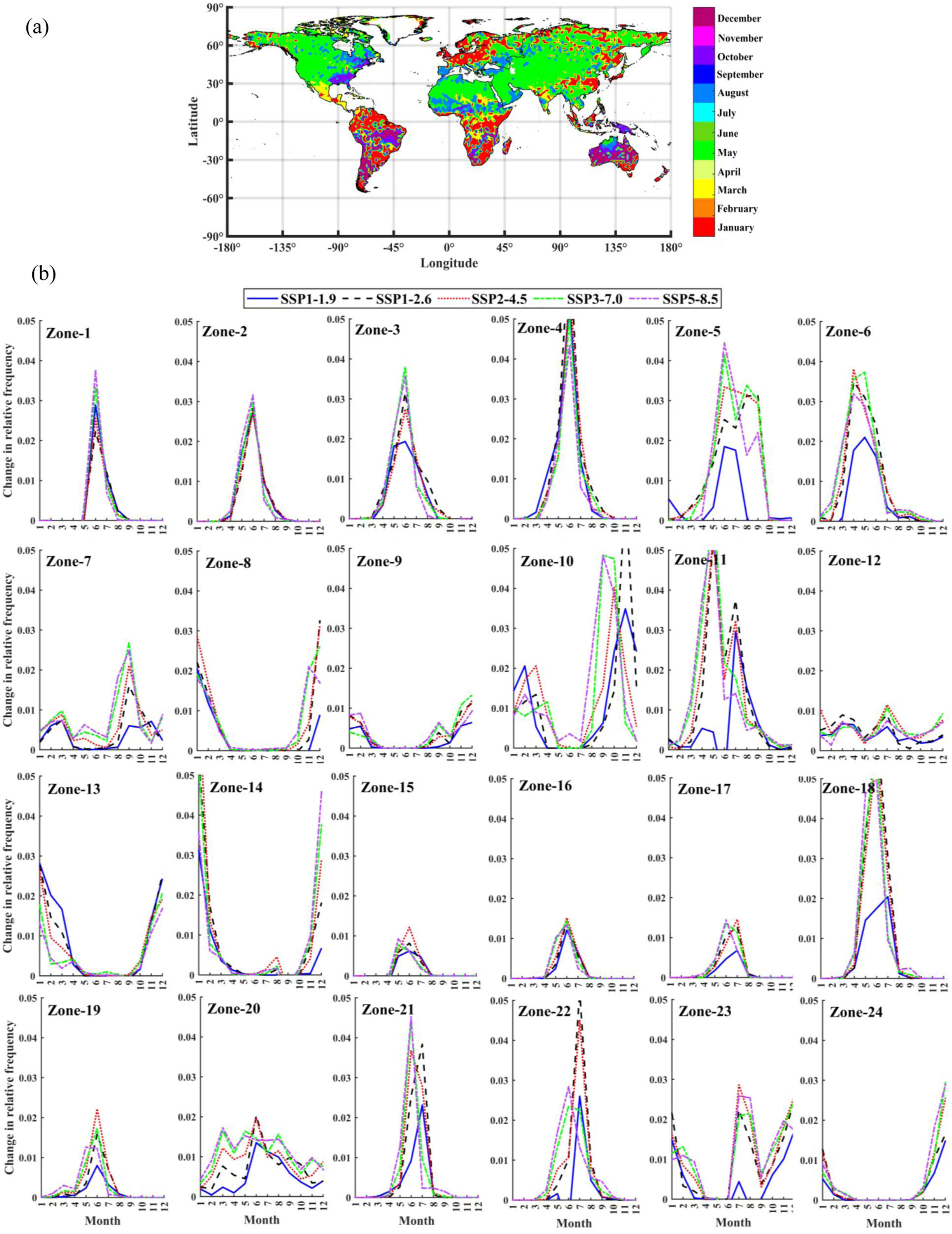

Fig. 5 Average monthly probability of experiencing MFDs across different parts of the globe for historical and future SSP forcing scenarios. **a** Months during which probability of experiencing MFDs was high in different parts of the globe during the historical period (1979–2014). **b** Projected monthly changes in the average probability (relative frequency) of experiencing MFDs (with respect to the historical period) across grids in different climate zones for future SSP forcing scenarios. The probabilities were determined based on MFDs identified from the multi-model ensemble.

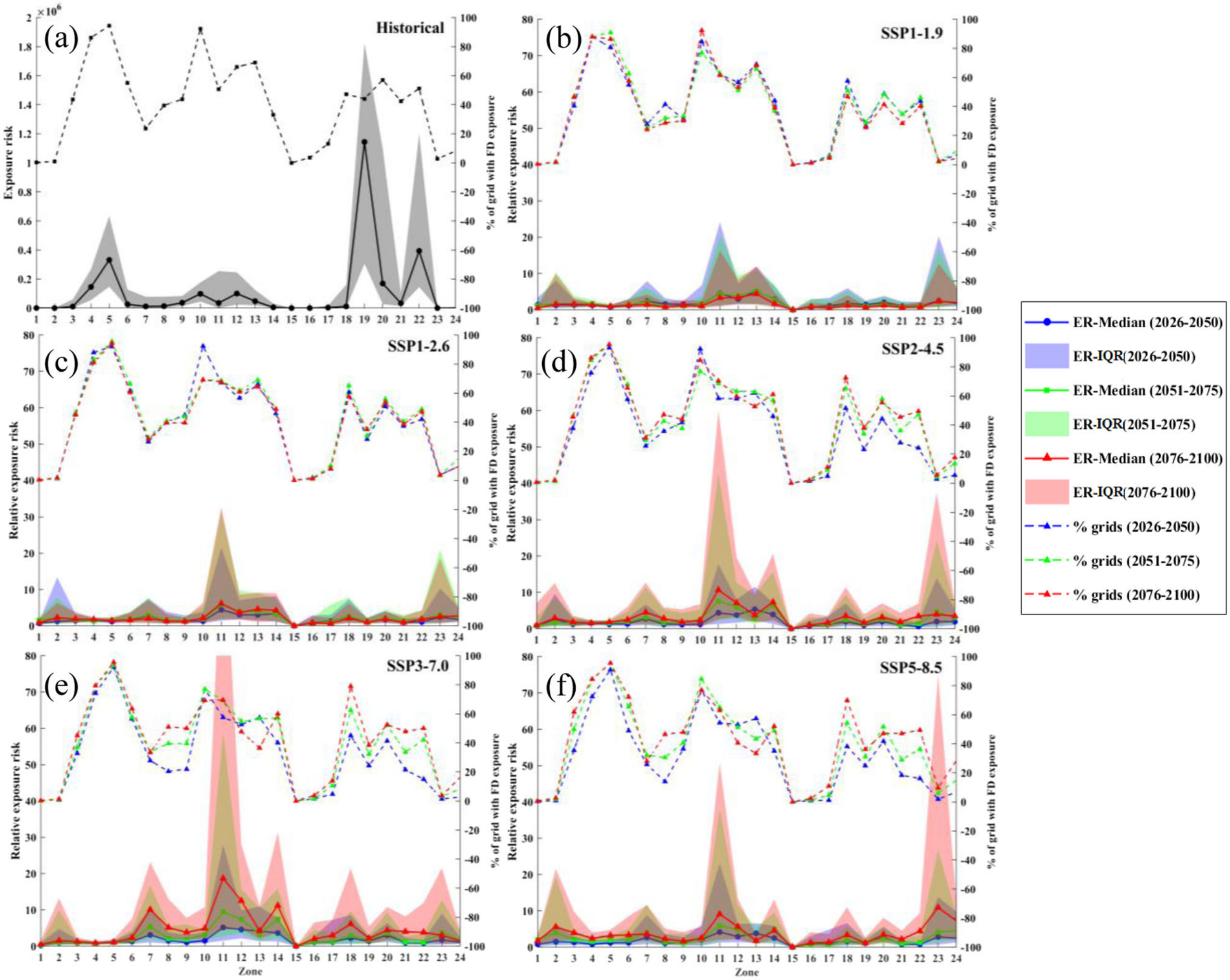

Fig. 6 Regional-scale exposure risk of MFDs for historical and future SSP-FS. **a** Historical period's median exposure risk (ER) and **b**–**f** the median relative ER corresponding to 5 future SSP forcing scenarios for 24 climate zones. The inter-quartile range (IQR) of ER and relative ER values across grids in each zone is shown as shaded area. The scale on the secondary vertical axis shows the percentage of grids in a zone (classified as hotspot regions of MFDs) having the ER greater than the threshold value (0.01 million days × persons per year). The ER was determined based on the MFD duration derived from the multi-model ensemble and the population data.

essential for their prediction to provide early warning for initiating appropriate mitigation measures. Towards this, 14 climate variables were considered as possible attributes and their influence on each of the predictors (i.e., precipitation, PET, and T_{avg}) during the MFD development period (i.e., 5 pentads preceding and another 5 pentads following the initialization of an event) was assessed for each climate zone. Daily records of those attributes were extracted from the 12 GCMs (Supplementary Table 7) and were resampled to the common resolution of 1.5°.

The assessment was done using 42 Spearman's correlation coefficients, each of which was for a different attribute-predictor pair. Each pair comprised one of the 14 climate variables and the standardized pentad mean of a predictor (precipitation, PET and T_{avg}) of MFD. For each attribute-predictor pair, the correlation was computed at each grid between 50 standardized daily values of the attribute and predictor corresponding to the days in 10 pentads identified for each MFD event. Subsequently, the arithmetic average of such correlation estimates obtained for all the MFD events at all the grids in the chosen region was computed. This statistic is henceforth referred to as γ_{ap}. The γ_{ap} values corresponding to the attribute-predictor pair were derived considering those GCMs which provided the daily scale data for the chosen attribute and predictor. The medians of the γ_{ap} estimates determined from multiple GCMs for each region were visually analyzed in the form of a correlation plot to discern the influence of the attribute on the predictor.

The most influencing attributes for each predictor favouring MFD development were identified for each climate zone from 14 hydroclimatic variables (Supplementary Table 7) by analyzing their corresponding γ_{ap} values. The analysis showed that the correlation strength between any chosen attribute and predictor varies across the zones. The attribute that has the most influence on temperature and PET anomalies across all zones is surface upwelling long-wave flux in the air (*rlus*) (Fig. 10a, b). Similarly, the attributes that highly influence precipitation anomalies are cloud area fraction (*clt*), specific humidity (*huss*), convective precipitation flux (*prc*), atmospheric water vapour content (*prw*), surface downwelling long-wave flux in the air (*rlds*), air pressure at sea level (*psl*), top of atmosphere outgoing long-wave flux (*rlut*), surface downwelling short-wave flux in the air (*rsds*), and surface upwelling short-wave flux in the air (*rsus*). The attributes *rlut*, *rsds*, *rsus* exhibit a negative correlation, whereas the others show a positive correlation with precipitation (Fig. 10c). MFDs could be predicted with a short lead time by considering the most influencing predictors, which vary across zones depending on their climate characteristics, to provide early MFD mitigation warnings.

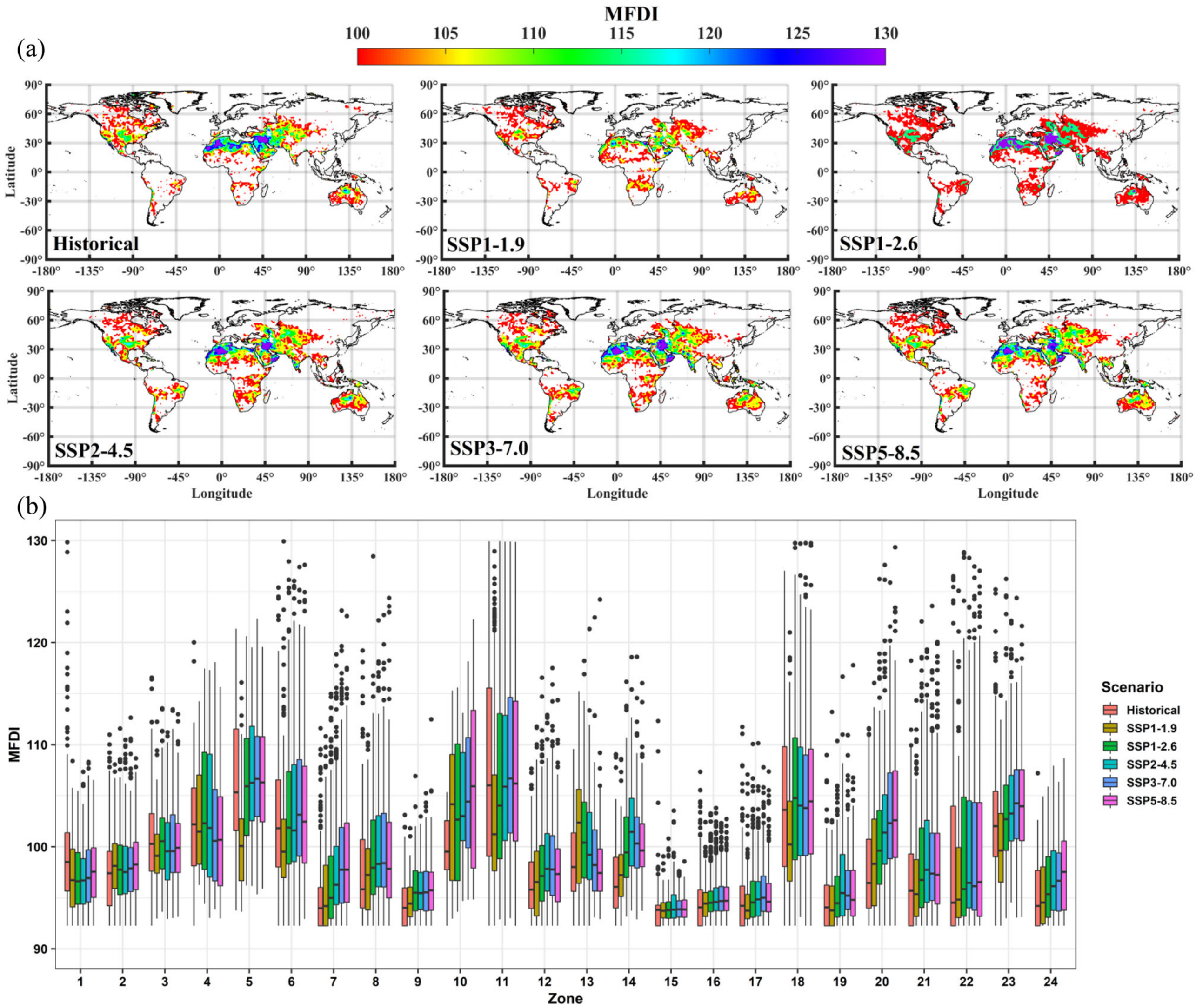

Fig. 7 Hotspot regions of MFDs identified using multivariate flash drought indicator (MFDI) for historical and future SSP forcing scenarios. a Global hotspot regions of MFDs identified using multivariate flash drought indicator (MFDI) for historical and future SSP forcing scenarios. The MFDI estimates were determined based on the FD characteristics derived from the multi-model ensemble prepared from 12 GCMs. **b** Boxplots, each showing the variation in MFDI values across grids in a climate zone for historical and 5 SSP-FS. Whiskers extend from the box to 5 and 95% quantiles on the lower and the upper side of the box, respectively. The horizontal line in the box represents the median, whereas the black dots represent outliers. The colour bars shown are valid across all the boxplots.

DISCUSSIONS

The changes in impacts and potential hotspot locations of MFDs were analyzed at regional- (considering 24 climate zones), continental- and global scales based on hydrometeorological information corresponding to the historical period and future SSP-FS. At the global scale, there is approximately an average increase of (i) 41.3 ± 12.1% in relative frequency, (ii) 45.7 ± 15.5% in duration, and (iii) 50.6 ± 14.6% in severity of MFDs with respect to the historical period across different SSP-FS. Similarly, the percentage of global land area exhibiting a positive trend in duration and critical severity of MFDs is also projected to rise, and the highest percentage increase in those characteristics were 26.9 and 29.3%, respectively, for the SSP5–8.5 scenario. MFDs are found to have the highest frequency/probability of occurrence during the summer season. Even though the number of years experiencing MFDs is projected to rise considerably, the annual count/frequency (1–2 times annually during the peak summer months) of MFDs is not projected to vary significantly in the future SSP-FS. Analysis of the exposure risk of MFDs shows that Africa is projected to be the highest affected by MFDs. The Indian subcontinent is projected to have the highest exposure risk due to increased population density and temperature due to rising GHG emissions. The MFD global hotspot regions were identified using MFDI for the historical period, and future SSP-FS, and it was noted that the hotspot areas are projected to increase for all future projections, with the highest increase for scenarios SSP3–7.0 and SSP5–8.5 (>20% increase globally). Moreover, the hotspots were more prominent in arid and semi-arid regions as the MFD impact increases with aridity (or decreases with aridity index). The increase in temperature and PET anomalies combined with a rapid decline in precipitation anomalies favours the initialization of MFDs. For the prediction of MFDs, hydrometeorological attributes that have the most influence on predictors (i.e., precipitation, PET, and temperature anomalies) of MFDs in the majority of the climate zones are *rlus*, *clt*, *huss*, *prc*, *prw*, *rlds*, *psl*, *rlut*, *rsds*, and *rsud*. The analysis of the vulnerability of different LULC classes showed that the susceptibility to MFDs is (i) highest for bare vegetation and (ii) least for herbaceous wetlands and forested regions. Furthermore, the highest MFD-vulnerable regions are found to be in lower elevation ranges (<1000 m).

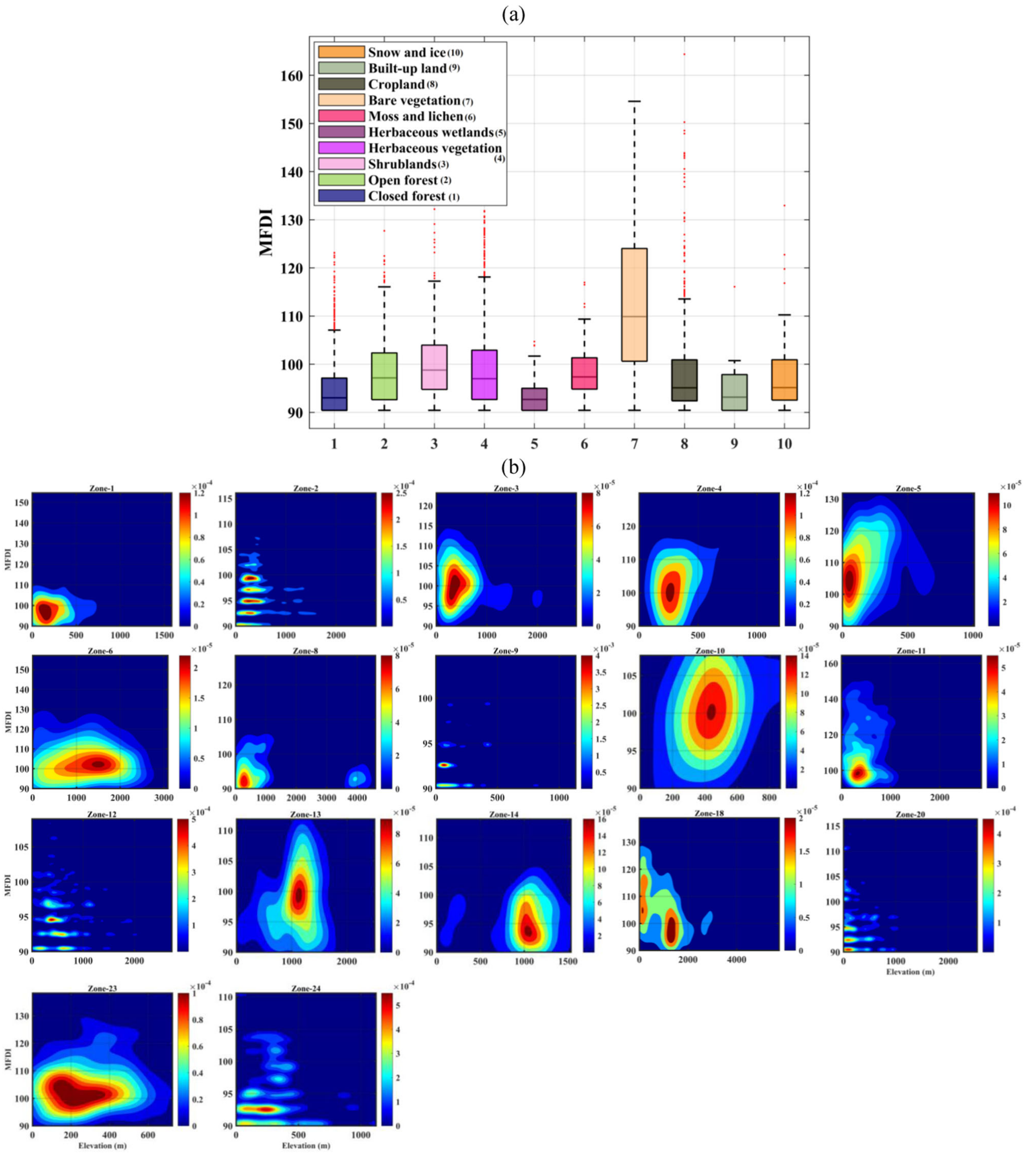

Fig. 8 Vulnerability of different land-use/landcover classes and elevation ranges to MFDs. a Variation of MFDI estimates for different land-use/land-cover classes across the global land area for the historical period. Whiskers extend from the box to 5 and 95% quantiles on the lower and the upper side of the box, respectively. The horizontal line in the box represents the median, whereas the red dots represent outliers. **b** Joint probability distribution of MFDI and elevation values for different climate classes covering the global land area for the historical period. Zones 7, 15–17, 19, 21, and 22 were not shown as those zones exhibited negligible influence with MFDs.

Effective forecast of MFDs and early warning systems with short lead time (e.g., pentad or sub-seasonal scale) is critical to successfully mitigate and prevent losses to different socio-economic sectors[35]. The hydrometeorological attributes identified to have the most influence on predictors of MFDs could be considered for forecasting MFDs at short lead-time to initiate mitigation activities. Apart from improving the MFD forecast capability, the operational framework of MFD mitigation could comprise of (i) identifying the hotspot regions based on estimates of MFD exposure risk and vulnerability, (ii) adopting structural (e.g., micro dams, ponds, wells, and other engineering projects) and non-structural (e.g., policies, operating practises) measures including MFD proofing programs, and (iii) increasing public awareness and community participation. Moreover, it is highly essential to

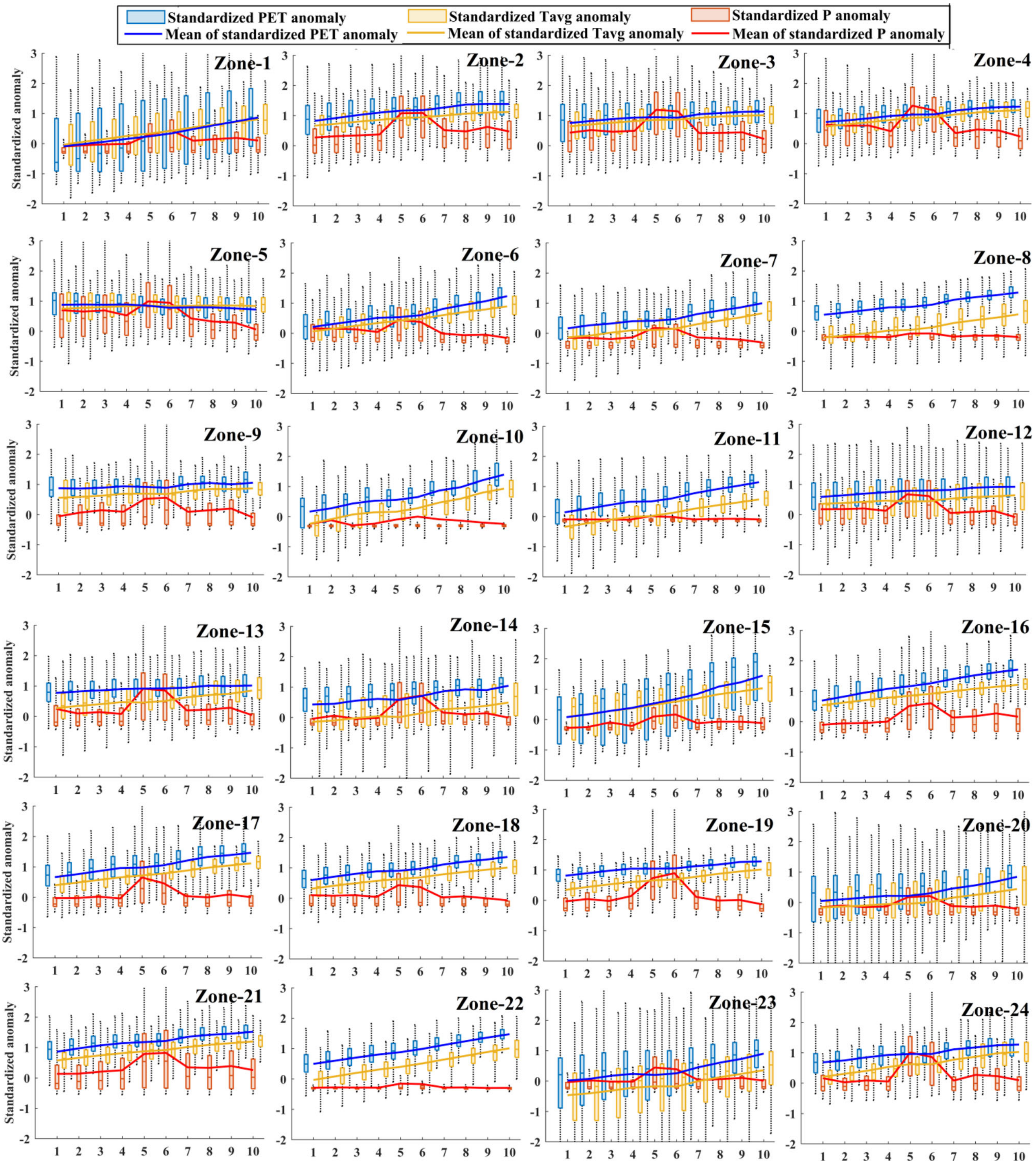

Fig. 9 Variation in pentad means of precipitation, potential evapotranspiration, and temperature anomalies for MFDs determined in 24 climate zones considering multi-model ensemble for the historical period. Variation in pentad means of precipitation (P), potential evapotranspiration (PET) and temperature (Tavg) anomalies for MFDs determined in 24 climate zones considering multi-model ensemble for the historical period (1979–2014). The horizontal axis shows ten pentads corresponding to a MFD event (5 pentads preceding and another 5 pentads following the initialization of the event). Each boxplot corresponds to one among the 10 pentads and it shows variation in the pentad's mean precipitation, PET or temperature noted across all grids in a zone over all MFD events. Whiskers extend from the box to 5 and 95% quantiles on the lower and the upper side of the box, respectively. The horizontal line in the box represents the median.

minimize the global warming effect (limiting global warming to 2 °C) by adopting appropriate measures (e.g., Paris agreement, 2015[36–38]), which can significantly reduce the impact of MFDs.

The analysis could be further extended to assess the impacts of agricultural FDs for future SSP-FS. It could also focus on the FD effects on agricultural yield and GDP (Gross Domestic Product) for present and future SSP-FS at global and regional scales. The climatological drivers of agricultural FDs at a regional scale can also be identified to provide early warning for drought mitigation. It has been noted from the present study that

(a) Predictor: Temperature anomalies

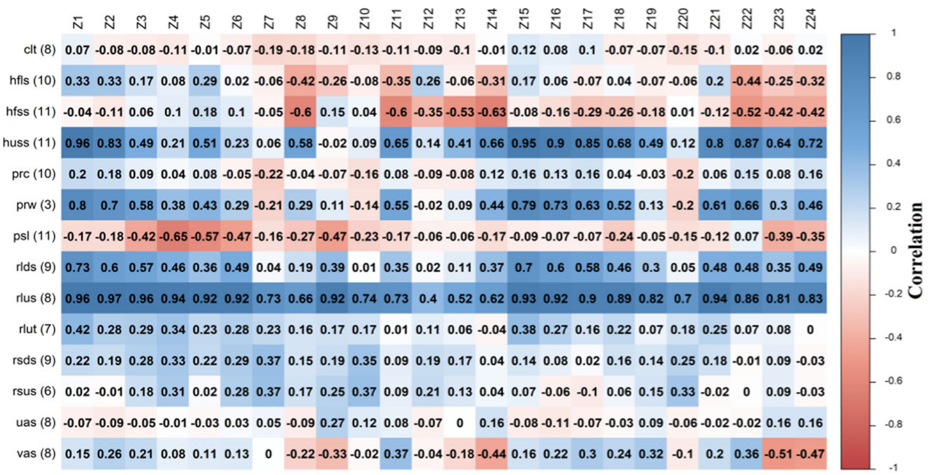

	Z1	Z2	Z3	Z4	Z5	Z6	Z7	Z8	Z9	Z10	Z11	Z12	Z13	Z14	Z15	Z16	Z17	Z18	Z19	Z20	Z21	Z22	Z23	Z24
clt (8)	0.07	-0.08	-0.08	-0.11	-0.01	-0.07	-0.19	-0.18	-0.11	-0.13	-0.11	-0.09	-0.1	-0.01	0.12	0.08	0.1	-0.07	-0.07	-0.15	-0.1	0.02	-0.06	0.02
hfls (10)	0.33	0.33	0.17	0.08	0.29	0.02	-0.06	-0.42	-0.26	-0.08	-0.35	0.26	-0.06	-0.31	0.17	0.06	-0.07	0.04	-0.07	-0.06	0.2	-0.44	-0.25	-0.32
hfss (11)	-0.04	-0.11	0.06	0.1	0.18	0.1	-0.05	-0.6	0.15	0.04	-0.6	-0.35	-0.53	-0.63	-0.08	-0.16	-0.29	-0.26	-0.18	0.01	-0.12	-0.52	-0.42	-0.42
huss (11)	0.96	0.83	0.49	0.21	0.51	0.23	0.06	0.58	-0.02	0.09	0.65	0.14	0.41	0.66	0.95	0.9	0.85	0.68	0.49	0.12	0.8	0.87	0.64	0.72
prc (10)	0.2	0.18	0.09	0.04	0.08	-0.05	-0.22	-0.04	-0.07	-0.16	0.08	-0.09	-0.08	0.12	0.16	0.13	0.16	0.04	-0.03	-0.2	0.06	0.15	0.08	0.16
prw (3)	0.8	0.7	0.58	0.38	0.43	0.29	-0.21	0.29	0.11	-0.14	0.55	-0.02	0.09	0.44	0.79	0.73	0.63	0.52	0.13	-0.2	0.61	0.66	0.3	0.46
psl (11)	-0.17	-0.18	-0.42	-0.65	-0.57	-0.47	-0.16	-0.27	-0.47	-0.23	-0.17	-0.06	-0.06	-0.17	-0.09	-0.07	-0.07	-0.24	-0.05	-0.15	-0.12	0.07	-0.39	-0.35
rlds (9)	0.73	0.6	0.57	0.46	0.36	0.49	0.04	0.19	0.39	0.01	0.35	0.02	0.11	0.37	0.7	0.6	0.58	0.46	0.3	0.05	0.48	0.48	0.35	0.49
rlus (8)	0.96	0.97	0.96	0.94	0.92	0.92	0.73	0.66	0.92	0.74	0.73	0.4	0.52	0.62	0.93	0.92	0.9	0.89	0.82	0.7	0.94	0.86	0.81	0.83
rlut (7)	0.42	0.28	0.29	0.34	0.23	0.28	0.23	0.16	0.17	0.17	0.01	0.11	0.06	-0.04	0.38	0.27	0.16	0.22	0.07	0.18	0.25	0.07	0.08	0
rsds (9)	0.22	0.19	0.28	0.33	0.22	0.29	0.37	0.15	0.19	0.35	0.09	0.19	0.17	0.04	0.14	0.08	0.02	0.16	0.14	0.25	0.18	-0.01	0.09	-0.03
rsus (6)	0.02	-0.01	0.18	0.31	0.02	0.28	0.37	0.17	0.25	0.37	0.09	0.21	0.13	0.04	0.07	-0.06	-0.1	0.06	0.15	0.33	-0.02	0	0.09	-0.03
uas (8)	-0.07	-0.09	-0.05	-0.01	-0.03	0.03	0.05	-0.09	0.27	0.12	0.08	-0.07	0	0.16	-0.08	-0.11	-0.07	-0.03	0.09	-0.06	-0.02	-0.02	0.16	0.16
vas (8)	0.15	0.26	0.21	0.08	0.11	0.13	0	-0.22	-0.33	-0.02	0.37	-0.04	-0.18	-0.44	0.16	0.22	0.3	0.24	0.32	-0.1	0.2	0.36	-0.51	-0.47

(b) Predictor: PET anomalies

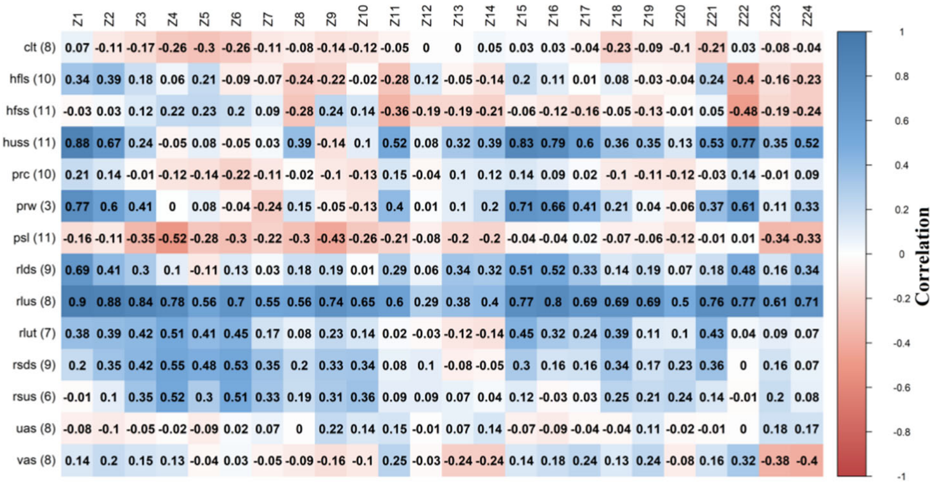

	Z1	Z2	Z3	Z4	Z5	Z6	Z7	Z8	Z9	Z10	Z11	Z12	Z13	Z14	Z15	Z16	Z17	Z18	Z19	Z20	Z21	Z22	Z23	Z24
clt (8)	0.07	-0.11	-0.17	-0.26	-0.3	-0.26	-0.11	-0.08	-0.14	-0.12	-0.05	0	0	0.05	0.03	0.03	-0.04	-0.23	-0.09	-0.1	-0.21	0.03	-0.08	-0.04
hfls (10)	0.34	0.39	0.18	0.06	0.21	-0.09	-0.07	-0.24	-0.22	-0.02	-0.28	0.12	-0.05	-0.14	0.2	0.11	0.01	0.08	-0.03	-0.04	0.24	-0.4	-0.16	-0.23
hfss (11)	-0.03	0.03	0.12	0.22	0.23	0.2	0.09	-0.28	0.24	0.14	-0.36	-0.19	-0.19	-0.21	-0.06	-0.12	-0.16	-0.05	-0.13	-0.01	0.05	-0.48	-0.19	-0.24
huss (11)	0.88	0.67	0.24	-0.05	0.08	-0.05	0.03	0.39	-0.14	0.1	0.52	0.08	0.32	0.39	0.83	0.79	0.6	0.36	0.35	0.13	0.53	0.77	0.35	0.52
prc (10)	0.21	0.14	-0.01	-0.12	-0.14	-0.22	-0.11	-0.02	-0.1	-0.13	0.15	-0.04	0.1	0.12	0.14	0.09	0.02	-0.1	-0.11	-0.12	-0.03	0.14	-0.01	0.09
prw (3)	0.77	0.6	0.41	0	0.08	-0.04	-0.24	0.15	-0.05	-0.13	0.4	0.01	0.1	0.2	0.71	0.66	0.41	0.21	0.04	-0.06	0.37	0.61	0.11	0.33
psl (11)	-0.16	-0.11	-0.35	-0.52	-0.28	-0.3	-0.22	-0.3	-0.43	-0.26	-0.21	-0.08	-0.2	-0.2	-0.04	-0.04	0.02	-0.07	-0.06	-0.12	-0.01	0.01	-0.34	-0.33
rlds (9)	0.69	0.41	0.3	0.1	-0.11	0.13	0.03	0.18	0.19	0.01	0.29	0.06	0.34	0.32	0.51	0.52	0.33	0.14	0.19	0.07	0.18	0.48	0.16	0.34
rlus (8)	0.9	0.88	0.84	0.78	0.56	0.7	0.55	0.56	0.74	0.65	0.6	0.29	0.38	0.4	0.77	0.8	0.69	0.69	0.69	0.5	0.76	0.77	0.61	0.71
rlut (7)	0.38	0.39	0.42	0.51	0.41	0.45	0.17	0.08	0.23	0.14	0.02	-0.03	-0.12	-0.14	0.45	0.32	0.24	0.39	0.11	0.1	0.43	0.04	0.09	0.07
rsds (9)	0.2	0.35	0.42	0.55	0.48	0.53	0.35	0.2	0.33	0.34	0.08	0.1	-0.08	-0.05	0.3	0.16	0.16	0.34	0.17	0.23	0.36	0	0.16	0.07
rsus (6)	-0.01	0.1	0.35	0.52	0.3	0.51	0.33	0.19	0.31	0.36	0.09	0.09	0.07	0.04	0.12	-0.03	0.03	0.25	0.21	0.24	0.14	-0.01	0.2	0.08
uas (8)	-0.08	-0.1	-0.05	-0.02	-0.09	0.02	0.07	0	0.22	0.14	0.15	-0.01	0.07	0.14	-0.07	-0.09	-0.04	-0.04	0.11	-0.02	-0.01	0	0.18	0.17
vas (8)	0.14	0.2	0.15	0.13	-0.04	0.03	-0.05	-0.09	-0.16	-0.1	0.25	-0.03	-0.24	-0.24	0.14	0.18	0.24	0.13	0.24	-0.08	0.16	0.32	-0.38	-0.4

(c) Predictor: Precipitation anomalies

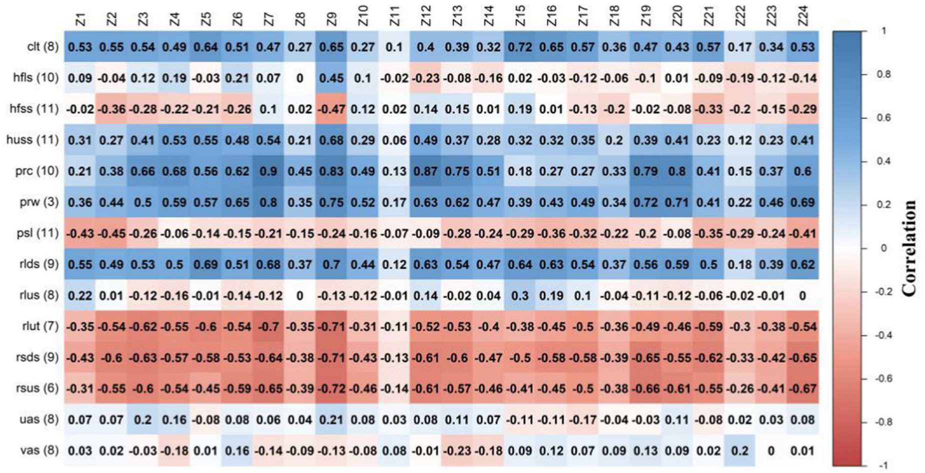

	Z1	Z2	Z3	Z4	Z5	Z6	Z7	Z8	Z9	Z10	Z11	Z12	Z13	Z14	Z15	Z16	Z17	Z18	Z19	Z20	Z21	Z22	Z23	Z24
clt (8)	0.53	0.55	0.54	0.49	0.64	0.51	0.47	0.27	0.65	0.27	0.1	0.4	0.39	0.32	0.72	0.65	0.57	0.36	0.47	0.43	0.57	0.17	0.34	0.53
hfls (10)	0.09	-0.04	0.12	0.19	-0.03	0.21	0.07	0	0.45	0.1	-0.02	-0.23	-0.08	-0.16	0.02	-0.03	-0.12	-0.06	-0.1	0.01	-0.09	-0.19	-0.12	-0.14
hfss (11)	-0.02	-0.36	-0.28	-0.22	-0.21	-0.26	0.1	0.02	-0.47	0.12	0.02	0.14	0.15	0.01	0.19	0.01	-0.13	-0.2	-0.02	-0.08	-0.33	-0.2	-0.15	-0.29
huss (11)	0.31	0.27	0.41	0.53	0.55	0.48	0.54	0.21	0.68	0.29	0.06	0.49	0.37	0.28	0.32	0.32	0.35	0.2	0.39	0.41	0.23	0.12	0.23	0.41
prc (10)	0.21	0.38	0.66	0.68	0.56	0.62	0.9	0.45	0.83	0.49	0.13	0.87	0.75	0.51	0.18	0.27	0.27	0.33	0.79	0.8	0.41	0.15	0.37	0.6
prw (3)	0.36	0.44	0.5	0.59	0.57	0.65	0.8	0.35	0.75	0.52	0.17	0.63	0.62	0.47	0.39	0.43	0.49	0.34	0.72	0.71	0.41	0.22	0.46	0.69
psl (11)	-0.43	-0.45	-0.26	-0.06	-0.14	-0.15	-0.21	-0.15	-0.24	-0.16	-0.07	-0.09	-0.28	-0.24	-0.29	-0.36	-0.32	-0.22	-0.2	-0.08	-0.35	-0.29	-0.24	-0.41
rlds (9)	0.55	0.49	0.53	0.5	0.69	0.51	0.68	0.37	0.7	0.44	0.12	0.63	0.54	0.47	0.64	0.63	0.54	0.37	0.56	0.59	0.5	0.18	0.39	0.62
rlus (8)	0.22	0.01	-0.12	-0.16	-0.01	-0.14	-0.12	0	-0.13	-0.12	-0.01	0.14	-0.02	0.04	0.3	0.19	0.1	-0.04	-0.11	-0.12	-0.06	-0.02	-0.01	0
rlut (7)	-0.35	-0.54	-0.62	-0.55	-0.6	-0.54	-0.7	-0.35	-0.71	-0.31	-0.11	-0.52	-0.53	-0.4	-0.38	-0.45	-0.5	-0.36	-0.49	-0.46	-0.59	-0.3	-0.38	-0.54
rsds (9)	-0.43	-0.6	-0.63	-0.57	-0.58	-0.53	-0.64	-0.38	-0.71	-0.43	-0.13	-0.61	-0.6	-0.47	-0.5	-0.58	-0.58	-0.39	-0.65	-0.55	-0.62	-0.33	-0.42	-0.65
rsus (6)	-0.31	-0.55	-0.6	-0.54	-0.45	-0.59	-0.65	-0.39	-0.72	-0.46	-0.14	-0.61	-0.57	-0.46	-0.41	-0.45	-0.5	-0.38	-0.66	-0.61	-0.55	-0.26	-0.41	-0.67
uas (8)	0.07	0.07	0.2	0.16	-0.08	0.08	0.06	0.04	0.21	0.08	0.03	0.08	0.11	0.07	-0.11	-0.11	-0.17	-0.04	-0.03	0.11	-0.08	0.02	0.03	0.08
vas (8)	0.03	0.02	-0.03	-0.18	0.01	0.16	-0.14	-0.09	-0.13	-0.08	0.08	-0.01	-0.23	-0.18	0.09	0.12	0.07	0.09	0.13	0.09	0.02	0.2	0	0.01

Fig. 10 Influence of 14 hydroclimatic attributes on MFD-related predictors for 24 climate zones. Influence of 14 hydroclimatic attributes on MFD-related predictors (**a** temperature, **b** PET, and **c** precipitation anomalies) for 24 climate zones (Z1 to Z24). Shown are the medians of correlation estimates corresponding to different attribute-predictor pairs. Each correlation estimate is based on a GCM, and the number of GCMs considered for each attribute-predictor pair is shown in parenthesis following abbreviation of the attribute (appearing along the vertical axis). Note- Attribute variables: clt-Cloud area fraction; hfls- Surface upward latent heat flux; hfss-Surface upward sensible heat flux; huss-Specific humidity; prc-Convective precipitation flux; prw- Atmospheric water vapour content; psl-Air pressure at sea level; rlds-Surface downwelling long-wave flux in air; rlus-Surface upwelling long-wave flux in air; rlut-Top of atmosphere outgoing long-wave flux; rsds-Surface downwelling short-wave flux in air; rsus-Surface upwelling short-wave flux in air; uas-Eastward wind; vas-Northward wind.

hydrometeorological/climatological factors play a significant role in the development of MFDs. One may attempt to consider a more diverse set of predictors than those analyzed in this study to identify potential predictors for use-in short lead time predictions of MFDs. Extensive future studies are essential in this direction at regional and local scales.

METHODS

Identification of MFDs

MFDs are identified using the SAPEI quantified at a pentad scale (5-day interval) utilizing precipitation and PET. The index accounts for antecedent water surplus/deficit reflecting wet/dry conditions[19], which can be determined for dth day ($d = 1, \ldots, L$) in a N-year long record as,

$$D_d = \sum_{n=0}^{N_A} \alpha^n \left(P_{d-n} - \mathrm{PET}_{d-n}\right), \alpha^{N_A} = c \qquad (1)$$

where N_A is the number of antecedent days, α is the decay constant whose value ranges from 0.8 to 0.98[39–42], and $c\left(P_{d-N_A} - \mathrm{PET}_{d-N_A}\right)$ is the contribution from water balance of the first day (among the N_A antecedent days) to D_d, P_{d-n}, and PET_{d-n} represent the daily precipitation and PET values for the (d-n)-th day. The PET estimates were obtained using Hargraves's method[43,44]. In this study, we have considered $\alpha = 0.98$ and $\mathbf{c} = 13\%$, resulting in $N_A = 100$ days as in the previous studies[39]. The computed $D_1, \ldots, D_L$ values were divided into disjoint 5-day sized windows (pentads), and the arithmetic average (pentad mean) of data points corresponding to each window k $(= 1, \ldots, L')$ was estimated and denoted as D'_k. Conventionally, drought indices are estimated by fitting a probability distribution to D'_k. However, estimating a drought index considering multiple GCM simulations with this procedure could be challenging as appropriate distribution may not be easily identifiable. Hence, the cumulative probability density of D'_k was obtained using a non-parametric KDE method[45,46], and it was then transformed to a standard normal variable (i.e., SAPEI) using the approximate transformation[47]. Values of SAPEI less than or equal to -1 indicate a drought condition.

The temporal change in SAPEI was calculated and standardized as follows,

$$\left(\Delta\mathrm{SAPEI}_{i',j',k}\right)_z = \frac{\Delta\mathrm{SAPEI}_{i',j',k} - \mu_{\Delta SAPEI_{i',j'}}}{\sigma_{\Delta SAPEI_{i',j'}}}, \quad k = 1, \ldots, (L'-1) \qquad (2)$$

where $\left(\Delta\mathrm{SAPEI}_{i',j',k}\right)_z$ is the standardized score of $\Delta\mathrm{SAPEI}_{i',j',k}$ that denotes the change in SAPEI from k-th pentad to $k+1$-th pentad for a grid point (i', j'), $\mu_{\Delta SAPEI_{i',j'}}$ and $\sigma_{\Delta SAPEI_{i',j'}}$ are estimates of mean and standard deviation determined from $(L'-1)$ values of $\Delta\mathrm{SAPEI}_{i',j'}$ for the grid location. $\left(\Delta\mathrm{SAPEI}_{i',j',k}\right)_z$ is henceforth referred to as $\Delta\mathrm{SAPEI}_z$ for ease of discussion.

MFD events at each chosen location/grid are identified using a multi-criterion-based methodology following the available guidelines[1,9,10,27,48]. The methodology considers the following four criteria, of which the first two focus on the impacts of droughts and the latter two focus on the rapid intensification characteristics of the droughts.

1. A MFD should have a minimum length of not less than 6 pentads (i.e., 30 days). In other words, the negative trend in SAPEI should continue for at least 30 days.
2. The SAPEI value corresponding to the last pentad at the termination of MFD should fall below the 20th percentile of L' SAPEI values for the chosen location.
3. The $\Delta\mathrm{SAPEI}_z$ values computed between individual pentads in a MFD must be less than or equal to 40th percentile of $(L'-1)$ values of $\Delta\mathrm{SAPEI}_z$ determined using Eq. (2). Utmost one $\Delta\mathrm{SAPEI}_z$ value can be allowed to deviate from this criterion.
4. The average of all the $\Delta\mathrm{SAPEI}_z$ values in a MFD must be less than the 25th percentile of $(L'-1)$ values of $\Delta\mathrm{SAPEI}_z$.

Criteria 1 and 2 eliminate short-term dry spells and identify MFDs that can cause significant impacts on the environment. Whereas criteria 3 and 4 ensure that the MFDs have an overall rapid development rate and are not significantly slowed down by temporary moderations of SAPEI due to meteorological anomalies (e.g., higher precipitation, lower temperature, more cloud cover, or lower wind speed)[1]. Following this procedure, MFD events were identified at each of the 1.5° grids covering the global land surface area for the historical period and future climate change scenarios.

Determination of MFD characteristics

Various MFD characteristics were analyzed to assess the impacts and changes in MFD events for various SSP-FS with respect to the historical period. The MFD characteristics considered include (i) relative frequency/probability of occurrence, (ii) severity, (iii) duration, (iv) spatiotemporal variability and (v) exposure risk of MFDs.

The relative frequencies are computed at annual and monthly scales. The annual relative frequency is defined as the ratio of the number of MFD years by the total number of years in the period analyzed. A year could be classified as an MFD year if at least one MFD occurs in the year. Whereas the monthly relative frequency for a chosen month m is computed as the ratio of the number of years experiencing at least one MFD during the month m divided by the total number of years considered in the analyzed period. The annual duration of MFD is determined as the total number of days experiencing MFDs in a year. The severity of an MFD is defined as the sum of SAPEI values corresponding to pentads in the entire MFD period. In this study, the annual critical severity (i.e., the maximum of severities corresponding to all MFDs occurring in a year) is considered to characterize the impact of MFDs. The MFD exposure risk[9] for each year is computed by multiplying the annual population by the annual duration of MFDs.

The inter-annual variability of MFDs is defined as the lack of uniformity or uncertainty of MFD events at the annual scale, which can be quantified using marginal entropy[49] as,

$$H^{\mathrm{ME}} = -\sum_{\upsilon=1}^{N} \frac{m_\upsilon}{S} \log_2\left[\frac{m_\upsilon}{S}\right], \text{ where } S = \sum_{\upsilon=1}^{N} m_\upsilon \qquad (3)$$

where N represents the number of years considered as the baseline period $m_\upsilon = 1$ if the year υ experiences at least one MFD and zero otherwise. When, $m_\upsilon = 0$, $H^{\mathrm{ME}}(\cdot)$ could be considered to be zero, which is consistent with a well-known limit[50] $\left(\underset{x\to 0}{Lt}\; x \log x = 0\right)$. The value of entropy H^{ME} ranges from 0 to $H_{\max}(= \log_2 N)$. Where $H = 0$ and $H = H_{\max}$ correspond to the situations where there is no uncertainty and maximum uncertainty (i.e., MFDs are equally likely to occur each year), respectively. A Standardized Variability Index (SVI) was used in this study to quantify the variability of MFD and is computed as follows,

$$\mathrm{SVI} = \frac{H_{\max} - H^{\mathrm{ME}}}{H_{\max}} \qquad (4)$$

SVI has values in the range of [0,1], where 0 and 1 denote the least variability and highest variability, respectively. Variability quantifies the lack of uniformity in the occurrence of MFDs. For example, if all years experience at least one MFD or no MFD (i.e., uniform distribution scenario), the probability of occurrence of the MFD is the same for all the years, indicating high uncertainty and low temporal variability of MFDs (i.e., SVI~0). The use of SVI to quantify the variability of precipitation, dryness, and wetness conditions and to develop homogeneous precipitation regions can be found in previous studies[51–53].

Mann–Kendall (MK) trend test[54,55] was considered to identify the trend in annual estimates of (i) relative frequency/probability of occurrence, (ii) critical severity, and (iii) duration of MFDs at each of the 1.5° resolution grids covering the entire global land area. The trend analysis was performed at grid scale and zonal/regional scale.

Identification of MFD hotspot regions

In order to assess the socio-economic impacts and identify hotspot areas of MFDs for historical and future SSP scenarios, a MFDI is considered[21]. The MFDI is a composite metric that combines the information of the mean values of the chosen MFD attributes (e.g., relative frequency, duration, severity, exposure risk) using the Mazziotta-Pareto Index[56–58] (MPI).

The MPI methodology involves (i) standardization of values of each of the MFD attributes across all the grids (by dividing by their respective standard deviation) to nullify the effect of differences in units of attributes, and (ii) estimation of MPI for each location/grid by pooling the standardized values of the attributes and their aggregation, as described below. Let

$$\mathbf{X} = \begin{bmatrix} \mathbf{X}'_1 \\ \vdots \\ \mathbf{X}'_{S'} \end{bmatrix}_{S'\times 1} = \begin{bmatrix} x^{(1)}_{1,1} & \cdots & x^{(1)}_{1,j} & \cdots & x^{(1)}_{1,m} \\ \vdots & & \vdots & & \vdots \\ x^{(1)}_{N,1} & \cdots & x^{(1)}_{N,j} & \cdots & x^{(1)}_{N,m} \\ \vdots & & \vdots & & \vdots \\ x^{(S')}_{1,1} & \cdots & x^{(S')}_{1,j} & \cdots & x^{(S')}_{1,m} \\ \vdots & & \vdots & & \vdots \\ x^{(S')}_{N,1} & \cdots & x^{(S')}_{N,j} & \cdots & x^{(S')}_{N,m} \end{bmatrix}_{(S'\times N)\times m} \tag{5}$$

where $x^{(s)}_{i,j}$ is jth MFD attribute corresponding to i-th grid for scenario s $(=1,\ldots,S')$, m represents the total number of MFD attributes, N denotes the number of 1.5° grids on the global land area and S' refers to the number of scenarios. In this study, $S'=6$ (i.e., historical, SSP1–1.9, SSP1–2.6, SSP2-4.5, SSP3–7.0, SSP5–8.5).

Form the standardized matrix $\mathbf{Z} = \left\{ z^{(s)}_{i,j} : i = 1,\ldots,N; j = 1,\ldots,m; s = 1,\ldots,S' \right\}$ using $\mathbf{X}$ as follows,

$$z^{(s)}_{i,j} = 100 \pm \frac{\left(x^{(s)}_{i,j} - M_j\right)}{\sigma_j} \times 10 \tag{6}$$

where M_j and σ_j denote the mean and standard deviation of elements in jth column of the matrix $\mathbf{Z}$. $z^{(s)}_{i,j}$ values obtained for different scenarios have a common scale with mean and standard deviation equal to 100 and 10, respectively. Both positive and negative signs are shown in the relationship. A positive sign was considered for all the MFD attributes/characteristics that positively correlate with the MFD impact. The attributes were aggregated to arrive at MPI as,

$$\mathrm{MPI}^{(s)}_i = M^{(s)}_{z_i}\left[1 \pm \left(\mathrm{cv}^{(s)}_{z_i}\right)^2\right] = M^{(s)}_{z_i} \pm \sigma^{(s)}_{z_i}\mathrm{cv}^{(s)}_{z_i} \tag{7}$$

where $M^{(s)}_{z_i}$, $\sigma^{(s)}_{z_i}$, and $\mathrm{cv}^{(s)}_{z_i}$ denote mean, standard deviation, and coefficient of variation of all $z^{(s)}_{i,j}$ values corresponding to grid i for scenario s. In this study, all the chosen attributes are such that adverse effects of MFD on socio-economic sectors increase with attributes' magnitude. Therefore, the sign of the penalty $\left(\left(\mathrm{cv}^{(s)}_{z_i}\right)^2\right)$ term was considered negative for computing $\mathrm{MPI}^{(s)}_i$, which is henceforth referred to as $\mathrm{MFDI}^{(s)}_i$. The value of MFDI generally ranges from 70 to 130, as the values of mean and standard deviation are chosen as 100 and 10 in Eq. (5). All the grid locations having MFDI values greater than 100 are declared as belonging to MFD hotspot region(s)[21]. To identify the hotspot regions for historical and future SSP-FS, the estimates of drought index (SAPEI) and the corresponding MFD characteristics are determined for each of the grids to form its attribute set.

Study area and data

The study assesses the MFD characteristics for the present and five future CMIP6 SSP-FS at global (all global land areas except Antarctica and Greenland), continental (6 continents), and regional (24 climate zones) scales. Twenty-four climate zones based on the Köppen climate classification system[59] (KCCS) were considered in this study to delve deeper into the regional scale characteristics of MFDs (Fig. 3). The KCCS divides climates into five main climate groups (tropical, dry, temperate, continental, and polar), with each group being divided based on seasonal precipitation and temperature patterns. Major hyper-arid and arid regions of the world fall in zones 4, 5, 6, 10, 11, 13, 14, 17, 18, 20, and 23, and polar regions fall in zones 1 and 15, respectively. Based on the study conducted by Christian et al., 2021[1], agricultural FD hotspot regions were mainly identified over Brazil (zone 7), the Sahel (zone 11), and India (zone 20), with notable hotspots over the central united states (zones 4 and 5), southwestern Russian (zone 21) and north-eastern China (zone 17).

MFDs are determined based on the daily-scale predictor variables (precipitation and maximum and minimum temperatures [Tmax and Tmin]) extracted from 12 GCMs (Supplementary Table 1) for the complete global land area. The GCMs are part of CMIP6. The scenarios considered in CMIP6 exemplify a range of future land-use changes and GHG emission scenarios based on integrated assessment models developed considering different assumptions regarding climate mitigation efforts, economic growth, and global governance. Considering these assumptions, SSPs were used to generate various radiative forcing levels and associated warmings at the end of the 21st century[60]. Simulations from 5 SSPs with r1i1p1f1 initial conditions were chosen to depict a range of possible future climate change scenarios. The SSPs include (i) SSP1–1.9 (very low GHG emissions), (ii) SSP1–2.6 (low GHG emissions) (iii) SSP2-4.5 (intermediate GHG emissions), (iv) SSP3–7.0 (high GHG emissions) and (v) SSP5–8.5 (very high GHG emissions) having a total anthropogenic forcing of +1.9, +2.6, +4.5, +7.0 and +8.5 Wm^{-2}, respectively. The 12 GCMs were chosen based on data availability for possible predictors and predictands for the historical (1979–2014) and five future (2015–2100) SSP-FS. In this study, CPC[61] daily data (precipitation, maximum and minimum temperature available at 0.5° resolution) for the period 1979–2014 are resampled to 1.5° resolution and are considered as the observed dataset.

Information on spatio-temporal distribution of global annual population was available at 0.5° resolution from ISIMIP-2b for the historical (1979–2014) and future periods (2015-2100) for SSP-1, -2, -3 and -5 scenarios. It was considered to arrive at the exposure risk of the population to MFDs. Fourteen climate variables (Supplementary Table 7) were considered as possible attributes of MFDs. Daily records of those attributes extracted from the 12 GCMs were considered to assess their regional scale influence on the predictors triggering MFD development. The datasets of these attribute variables and population were resampled to 1.5° resolution. The information on global elevation data and LULC were extracted from 30 m resolution Shuttle Radar Topography Mission (SRTM) Digital Elevation Model (SRTM-DEM) and 100 m resolution Copernicus global land services Land cover (CGLS-LC, 2015) map, respectively.

DATA AVAILABILITY

Readers can procure the (i) hydroclimatic data for historical and future SSP-FS from CMIP6 (https://esgf-node.llnl.gov/projects/cmip6/) (ii) unified gauge-based gridded precipitation and temperature data from CPC, NOAA/OAR/ESRL PSL, Boulder, Colorado, USA (https://psl.noaa.gov/data/gridded/data.cpc.globalprecip.html; https://psl.noaa.gov/data/gridded/data.cpc.globaltemp.html), (iii) population data from ISMIP2b (https://www.isimip.org/), (iv) 100 m resolution CGLS-LC map from Copernicus global land services (https://land.copernicus.eu/global/products/lc) and (v) 30 m SRTM-DEM from United States Geological Survey (https://www.usgs.gov).

CODE AVAILABILITY

The source codes for the analysis of this study are available from the corresponding author upon reasonable request.

Received: 7 April 2022; Accepted: 30 September 2022;
Published online: 15 October 2022

REFERENCES

1. Christian, J. I. et al. Global distribution, trends, and drivers of flash drought occurrence. *Nat. Commun.* **12**, 1–11 (2021).
2. Sharma, S. et al. Projected drought conditions over Southern slope of the Central Himalaya using CMIP6 models. *Earth Syst. Environ.* **5**, 849–859 (2021).
3. Almazroui, M. et al. Projected changes in climate extremes using CMIP6 simulations over SREX regions. *Earth Syst. Environ.* **5**, 481–497 (2021).
4. Chen, S. & Yuan, X. CMIP6 projects less frequent seasonal soil moisture droughts over China in response to different warming levels. *Environ. Res. Lett.* **16**, 044053 (2021).
5. Mo, K. C. & Lettenmaier, D. P. Heat wave flash droughts in decline. *Geophys. Res. Lett.* **42**, 2823–2829 (2015).
6. Mo, K. C. & Lettenmaier, D. P. Precipitation deficit flash droughts over the United States. *J. Hydrometeorol.* **17**, 1169–1184 (2016).
7. Hobbins, M. T. et al. The evaporative demand drought index. Part I: Linking drought evolution to variations in evaporative demand. *J. Hydrometeorol.* **17**, 1745–1761 (2016).
8. Hunt, E. D., Hubbard, K. G., Wilhite, D. A., Arkebauer, T. J. & Dutcher, A. L. The development and evaluation of a soil moisture index. *Int. J. Climatol.: A J. R. Meteorol. Soc.* **29**, 747–759 (2009).
9. Yuan, X. et al. Anthropogenic shift towards higher risk of flash drought over China. *Nat. Commun.* **10**, 1–8 (2019).
10. Mahto, S. S. & Mishra, V. Dominance of summer monsoon flash droughts in India. *Environ. Res. Lett.* **15**, 104061 (2020).
11. Noguera, I., Domínguez-Castro, F. & Vicente-Serrano, S. M. Flash drought response to precipitation and atmospheric evaporative demand in spain. *Atmosphere* **12**, 165 (2021).
12. Hunt, E. D. et al. Monitoring the effects of rapid onset of drought on non-irrigated maize with agronomic data and climate-based drought indices. *Agric. For. Meteorol.* **191**, 1–11 (2014).
13. Noguera, I., Domínguez-Castro, F. & Vicente-Serrano, S. M. Characteristics and trends of flash droughts in Spain, 1961–2018. *Ann. N. Y. Acad. Sci.* **1472**, 155–172 (2020).
14. Anderson, M. C., Norman, J. M., Mecikalski, J. R., Otkin, J. A. & Kustas, W. P. A climatological study of evapotranspiration and moisture stress across the continental United States based on thermal remote sensing: 1. Model formulation. *J. Geophys. Res.: Atmos.* **112**, D10117 (2007).
15. Anderson, M. C. et al. Evaluation of drought indices based on thermal remote sensing of evapotranspiration over the continental United States. *J. Clim.* **24**, 2025–2044 (2011).
16. Anderson, M. C. et al. An intercomparison of drought indicators based on thermal remote sensing and NLDAS-2 simulations with US Drought Monitor classifications. *J. Hydrometeorol.* **14**, 1035–1056 (2013).
17. Anderson, M. C. et al. Comparison of satellite-derived LAI and precipitation anomalies over Brazil with a thermal infrared-based Evaporative Stress Index for 2003–2013. *J. Hydrol.* **526**, 287–302 (2015).
18. Sun, Y. et al. Drought onset mechanisms revealed by satellite solar-induced chlorophyll fluorescence: Insights from two contrasting extreme events. *J. Geophys. Res.: Biogeosci.* **120**, 2427–2440 (2015).
19. Mishra, V., Bhatia, U. & Tiwari, A. D. Bias-corrected climate projections for South Asia from coupled model intercomparison project-6. *Sci. Data* **7**, 1–13 (2020).
20. Almazroui, M. et al. Assessment of CMIP6 performance and projected temperature and precipitation changes over South America. *Earth Syst. Environ.* **5**, 155–183 (2021).
21. Mukherjee, S. & Mishra, A. K. A multivariate flash drought indicator for identifying global hotspots and associated climate controls. *Geophys. Res. Lett.* **49**, e2021GL096804 (2022).
22. Parker, T., Gallant, A., Hobbins, M. & Hoffmann, D. Flash drought in Australia and its relationship to evaporative demand. *Environ. Res. Lett.* **16**, 064033 (2021).
23. Frieler, K. et al. Assessing the impacts of 1.5 C global warming–simulation protocol of the Inter-Sectoral Impact Model Intercomparison Project (ISIMIP2b). *Geosci. Model Dev.* **10**, 4321–4345 (2017).
24. Mishra, V., Aadhar, S., Asoka, A., Pai, S. & Kumar, R. On the frequency of the 2015 monsoon season drought in the Indo-Gangetic Plain. *Geophys. Res. Lett.* **43**, 102–12,112 (2016). 12.
25. Mishra, V., Smoliak, B. V., Lettenmaier, D. P. & Wallace, J. M. A prominent pattern of year-to-year variability in Indian Summer Monsoon Rainfall. *Proc. Natl Acad. Sci. USA* **109**, 7213–7217 (2012).
26. Roxy, M. K. et al. Drying of Indian subcontinent by rapid Indian Ocean warming and a weakening land-sea thermal gradient. *Nat. Commun.* **6**, 7423 (2015).
27. Mishra, V., Aadhar, S. & Mahto, S. S. Anthropogenic warming and intraseasonal summer monsoon variability amplify the risk of future flash droughts in India. *Npj Clim. Atmos. Sci.* **4**, 1–10 (2021).
28. Gadgil, S. & Gadgil, S. The Indian monsoon, GDP and agriculture. *Econ. Polit. Wkly.* **41**, 4887–4895 (2006).
29. Mishra, V., Thirumalai, K., Singh, D. & Aadhar, S. Future exacerbation of hot and dry summer monsoon extremes in India. *npj Clim. Atmos. Sci.* **3**, 10 (2020).
30. Krishna Kumar, K., Hoerling, M. & Rajagopalan, B. Advancing Indian monsoon rainfall predictions. *Geophys. Res. Lett.* **32**, 1–4 (2005).
31. Tsendbazar, N. E. et al. Copernicus Global Land Service: Land Cover 100m: Version 3 Globe 2015–2019: Validation Report; Zenodo, Geneve, Switzerland, https://land.copernicus.eu/global/products/lc (2020).
32. Bowler, D. E., Buyung-Ali, L., Knight, T. M. & Pullin, A. S. Urban greening to cool towns and cities: A systematic review of the empirical evidence. *Landsc. Urban Plan.* **97**, 147–155 (2010).
33. Rahman, M. A. et al. Traits of trees for cooling urban heat islands: A meta-analysis. *Build. Environ.* **170**, 106606 (2020).
34. Winbourne, J. B. et al. Tree transpiration and urban temperatures: Current understanding, implications, and future research directions. *BioScience* **70**, 576–588 (2020).
35. Otkin, J. A. et al. Flash droughts: A review and assessment of the challenges imposed by rapid-onset droughts in the United States. *Bull. Am. Meteorol. Soc.* **99**, 911–919 (2018).
36. Streck, C., Keenlyside, P. & Von Unger, M. The Paris Agreement: A new beginning. *J. Eur. Environ. Plan. Law* **13**, 3–29 (2016).
37. Schleussner, C. F. et al. Science and policy characteristics of the Paris Agreement temperature goal. *Nat. Clim. Change* **6**, 827–835 (2016).
38. Falkner, R. The Paris Agreement and the new logic of international climate politics. *Int. Aff.* **92**, 1107–1125 (2016).
39. Li, J. et al. Toward monitoring short-term droughts using a novel daily scale, standardized antecedent precipitation evapotranspiration index. *J. Hydrometeorol.* **21**, 891–908 (2020).
40. Lu, E. et al. The day-to-day monitoring of the 2011 severe drought in China. *Clim. Dyn.* **43**, 1–9 (2014).
41. Lu, E. Determining the start, duration, and strength of flood and drought with daily precipitation: Rationale. *Geophys. Res. Lett.* **36,** L12707 (2009).
42. Heggen, R. J. Normalized antecedent precipitation index. *J. Hydrologic Eng.* **6**, 377–381 (2001).
43. Hargraves, G. H. & Samani, Z. A. Estimating PET, Tech Note. *J. Irrig. Drain. Eng.* **vo. 108**, 225–230 (1982). no. 3.
44. Hargraves, G. H. & Samani, Z. A. Reference crop evapotranspiration from temperature. *Appl. Eng. Agric.* **1**, 96–99 (1985). no. 2.
45. Parzen, E. On estimation of a probability density function and mode. *Ann. Math. Stat.* **33**, 1065–1076 (1962).
46. Rosenblatt, M. Remarks on some non-parametric estimates of a density function. *Ann. Math. Stat.* **27**, 832–837 (1956).
47. Abramowitz, M., & Stegun, I. A. *Handbook of Mathematical Functions with Formulas, Graphs, and Mathematical Table* (US Department of Commerce, National Bureau of Standards, 1965).
48. Christian, J. I. et al. A methodology for flash drought identification: Application of flash drought frequency across the United States. *J. Hydrometeorol.* **20**, 833–846 (2019).
49. Maruyama, T., Kawachi, T. & Singh, V. P. Entropy-based assessment and clustering of potential water resources availability. *J. Hydrol.* **309**, 104–113 (2005).

50. Xu, H. et al. Entropy theory based multi-criteria resampling of rain gauge networks for hydrological modelling–A case study of humid area in southern China. *J. Hydrol.* **525**, 138–151 (2015).
51. Guntu, R. K., Rathinasamy, M., Agarwal, A. & Sivakumar, B. Spatiotemporal variability of Indian rainfall using multiscale entropy. *J. Hydrol.* **587**, 124916 (2020).
52. Guntu, R. K., Maheswaran, R., Agarwal, A. & Singh, V. P. Accounting for temporal variability for improved precipitation regionalization based on self-organizing map coupled with information theory. *J. Hydrol.* **590**, 125236 (2020b).
53. Sreeparvathy, V. & Srinivas, V. V. Global assessment of spatiotemporal variability of wet, normal, and dry conditions using multiscale entropy-based approach. *Sci. Rep.* **12**, 1–18 (2022).
54. Mann, H. B. Non-parametric tests against trend. *Econometrica: J. Econometric Soc.***13**, 245–259 (1945).
55. Kendall, M. G. *Rank Correlation Methods* 2nd edn (Charles Griffin and Company Ltd., 1975).
56. De Muro, P., Mazziotta, M. & Pareto, A. Composite indices of development and poverty: An application to MDGs. *Soc. Indic. Res.* **104**, 1–18 (2011).
57. Greco, S., Ishizaka, A., Tasiou, M. & Torrisi, G. On the methodological framework of composite indices: A review of the issues of weighting, aggregation, and robustness. *Soc. Indic. Res.* **141**, 61–94 (2019).
58. Mazziotta, M. & Pareto, A. On a generalized non-compensatory composite index for measuring socio-economic phenomena. *Soc. Indic. Res.* **127**, 983–1003 (2016).
59. Köppen, W. Die Wärmezonen der Erde, nach der Dauer der heissen, gemässigten und kalten Zeit und nach der Wirkung der Wärme auf die organische Welt betrachtet. *Meteorologische Z.* **1**, 5–226 (1884).
60. Gidden, M. J. et al. Global emissions pathways under different socio-economic scenarios for use in CMIP6: A dataset of harmonized emissions trajectories through the end of the century. *Geosci. Model Dev.* **12**, 1443–1475 (2019).
61. Xie, P., Chen, M. & Shi, W. CPC unified gauge-based analysis of global daily precipitation. In *Preprints, 24th Conf. on Hydrology*, Atlanta, GA, *Amer. Meteor. Soc*, Vol. 2 (2010).

ACKNOWLEDGEMENTS

The authors wish to acknowledge the editor and two reviewers for their detailed and insightful reviews providing constructive comments and helpful suggestions. They also express their sincere gratitude to all the organizations whose data were considered in the present study. The authors also acknowledge the Ministry of Earth Sciences for the support provided through Project No. MoES/PAMC/H&C/41/2013-PC-II.

AUTHOR CONTRIBUTIONS

V.S.: Conceptualization, methodology, software, investigation, formal analysis, data curation, visualization, and validation. Writing-review and editing. V.V.S.: Conceptualization, methodology, validation, supervision, project administration, funding acquisition, resources, review, and editing.

COMPETING INTERESTS

The authors declare no competing interests.

ADDITIONAL INFORMATION

Supplementary information The online version contains supplementary material available at https://doi.org/10.1038/s41612-022-00302-1.

Correspondence and requests for materials should be addressed to Vijay Sreeparvathy.

Reprints and permission information is available at http://www.nature.com/reprints

Publisher's note Springer Nature remains neutral with regard to jurisdictional claims in published maps and institutional affiliations.